REVIEW ARTICLE

Off-resonance artifact correction for MRI: A review

Melissa W. Haskell[1,2] 🆔 | Jon-Fredrik Nielsen[3] | Douglas C. Noll[3]

[1]Electrical Engineering and Computer Science, University of Michigan, Ann Arbor, Michigan, USA

[2]Hyperfine Research, Guilford, Connecticut, USA

[3]Biomedical Engineering, University of Michigan, Ann Arbor, Michigan, USA

Correspondence
Melissa W. Haskell, Electrical Engineering and Computer Science, University of Michigan, Ann Arbor, MI, United States.
Email: mhaskell@hyperfine.io

In magnetic resonance imaging (MRI), inhomogeneity in the main magnetic field used for imaging, referred to as off-resonance, can lead to image artifacts ranging from mild to severe depending on the application. Off-resonance artifacts, such as signal loss, geometric distortions, and blurring, can compromise the clinical and scientific utility of MR images. In this review, we describe sources of off-resonance in MRI, how off-resonance affects images, and strategies to prevent and correct for off-resonance. Given recent advances and the great potential of low-field and/or portable MRI, we also highlight the advantages and challenges of imaging at low field with respect to off-resonance.

1 | INTRODUCTION

Magnetic resonance imaging (MRI) is an important clinical tool for diagnosis and intervention, as well as the leading modality for non-invasively imaging the *in vivo* human brain. At the core of the MRI experiment is a polarizing magnetic field, referred to as the B_0 field or the main magnetic field, that aligns the magnetic spins within an object. These spins will precess at a resonant frequency linearly proportional to the external B_0 field, and in the majority of MRI experiments it is ideal to have as homogeneous a B_0 field as possible so that all spins precess at the same frequency. In practice, many factors can lead to B_0 inhomogeneity, thus leading to a non-uniform precession frequency of the spins, and this is called *off-resonance*. Off-resonance can lead to artifacts in MR images, including signal loss, geometric distortions, and blurring.

Off-resonance artifacts have been reported since the early days of clinical MRI, along with the problems they present in interpreting MR images.[1–3] Geometric distortions that warp the shape of the anatomy create challenges in many clinical applications, including stereotactic localization,[4] MRI-guided biopsy,[5] and MRI-guided radiation therapy.[6,7] Metal implants can lead to severe geometric distortions, and also can create a total loss of signal around the metal object.[8] In MRI-based neuroscience research, uncorrected off-resonance artifacts can lead to a loss in quality of data, most notably in the field of functional MRI (fMRI).[9,10]

Because of these problems, many approaches exist in MRI workflows to mitigate off-resonance artifacts. Magnetic field shimming, where dedicated shim coils apply additional fields to offset and cancel out main field inhomogeneity, is automated and standard from most vendors. From a sequence perspective, one of the simplest solutions to avoid signal loss from off-resonance is to use spin-echo-based sequences,[11,12] which refocus signal at the echo time (TE). The expanded use of parallel imaging[13,14] has also allowed for smaller voxels in standard imaging protocols. Smaller voxels reduce signal loss because the magnetic fields within the voxels have less variation in frequency, hence less signal cancellation. There is also less B_0 distortion with parallel imaging, because data can be acquired in shorter readouts with higher effective bandwidths in *k*-space.

However, not all B_0 artifacts can be avoided with these approaches. Inside the human body, the magnetic field off-resonance map, called a B_0 *fieldmap* or *fieldmap* for short, often has spatial variations that are of much higher order than the second-order spherical harmonic shim corrections available on some systems, leaving the potential for residual off-resonance in hard to shim anatomy. Additionally, certain sequences require

gradient echo imaging with longer readouts to generate the desired image contrast or acquisition speed, and are therefore more prone to off-resonance artifacts (e.g., echo planar imaging (EPI)[15]). Longer TE times are important for sequences such as blood oxygen level dependent (BOLD) contrast fMRI,[16] to allow dephasing of the spins to present as T_2^* contrast. Susceptibility-weighted imaging (SWI) and quantitative susceptibility mapping (QSM) also require longer TE times to generate magnetic susceptibility contrast, and these sequences are useful tools to investigate pathologies such as intracranial hemorrhage, traumatic brain injury, stroke, neoplasm, and multiple sclerosis.[17,18] Further, even when the desired contrast does allow for the use of spin echo imaging and most B_0-induced signal loss can be avoided, geometric distortions can still be present due to unwanted gradients that add to the imaging gradients, resulting in k-space encoding errors.

It is also important to consider off-resonance artifacts and potential correction strategies when working with MRI scanners that have more inhomogeneous B_0 fields than high-field superconducting magnets. Recently, there have been many advances in portable MRI at lower fields to perform *in vivo* human imaging.[19–23] These new technologies are important for increasing the accessibility of MRI,[24] but they generally have less uniform B_0 fields than superconducting magnets and off-resonance correction approaches are needed. Low-field MRI scanners built with permanent magnets can also experience large field drifts due to temperature-induced field changes, so dynamic tracking of the B_0 field strength is sometimes needed during imaging.

This review is structured by first describing the sources of off-resonance in MRI in Section 2 and their effects on imaging in Section 3. Section 4 details ways to estimate a B_0 fieldmap using pulse sequence, hardware, and optimization-based approaches. Section 5 discusses strategies to prevent and correct for B_0 artifacts, and Section 6 concludes the paper. All code for the simulations shown here is available online at https://github.com/fmrilab/B0-review-2022, including example code to perform model-based image reconstruction (MBIR)[25] that incorporates a B_0 fieldmap[26] using the Michigan Image Reconstruction Toolbox (MIRT).[27]

2 | SOURCES OF MAGNETIC FIELD OFF-RESONANCE

2.1 | Main field inhomogeneity

2.1.1 | Modern superconducting magnet homogeneity

The B_0 polarizing fields of modern high-field superconducting magnets, most often at field strengths of 1.5 T or 3 T, are generally very uniform, and after shimming with superconducting shim coils and passive shim elements are of the order of 1 ppm (parts per million) uniformity over a large imaging volume. Because of this, artifacts from susceptibility, chemical shift, and metal implants (discussed in later sections) are the dominant sources of B_0 artifacts in high-field superconducting MRI scanners, and off-resonance artifacts from the magnet itself are minimal.

2.1.2 | New magnet designs for lower cost and portability

As more light-weight, low-cost, and portable MRI designs are being developed, permanent magnets and resistive electromagnets are being chosen to create the polarizing fields. Both permanent and resistive magnet designs are much less expensive to produce than superconducting magnets, and, importantly, are much less expensive and easier to operate and maintain. However, these magnets are generally less spatially homogeneous and may require B_0 field correction even for routine imaging. Permanent magnets have the advantage that they require no power or cooling mechanism to operate, but they can be very sensitive to temperature-induced field drifts, which often need to be monitored during scanning. Resistive magnets are not as temperature sensitive, but power consumption and cooling will need to be taken into consideration and will potentially limit the field strength and homogeneity.

There are examples in both industry and academia of newer permanent magnetic designs. Currently available commercially scanners include a 64 mT portable brain scanner (https://www.hyperfine.io), a 1 T scanner for the neonatal intensive care unit (https://www.aspectimaging.com), and a low-field system for dedicated prostate imaging and biopsy guidance (https://promaxo.com). Academic groups have created permanent magnet designs using cylindrical Halbach geometries,[28–30] dipole magnet geometries,[19,20] and single-sided designs.[31] Unlike superconducting magnets, these scanners have field homogeneities in the range of tens of ppm (for smaller field of view (FOV) extremity imaging) to hundreds or thousands of ppm for head imaging, but have been shown to successfully image human subjects.[19–22]

Resistive magnets at low field have also been explored. Obungoloch et al. designed and constructed a prepolarized MRI scanner that acquired phantom images at 2.66 mT with a polarizing field of 27 mT, and a field homogeneity of 5000 ppm, similar to the level of inhomogeneity in the permanent magnet Halbach designs.[32]

2.2 | Magnetic susceptibility

One of the largest sources of B_0 inhomogeneity during routine *in vivo* MRI is magnetic susceptibility (Figure 1). Magnetic susceptibility (sometimes called volume magnetic susceptibility),[33] denoted as χ, is the property of a material to either strengthen ($\chi > 0$) or weaken ($\chi < 0$) an applied magnetic field, based on its internal magnetic polarization, M, as follows:

$$\chi = M/B_0. \tag{1}$$

Magnetic susceptibility is unitless since it is the ratio of two fields, but it is often expressed in ppm for convenience in the context of MRI. For example, molecular oxygen, O_2, has a magnetic susceptibility of roughly $+1$ ppm, which means that when in the presence of a 1.5 T, or 64 MHz, external magnetic field, its internal polarization will be roughly 1.5 µT, or 64 Hz.

If an object has non-uniform magnetic susceptibility, it will lead to a non-uniform magnetic field, even within the most uniform of applied fields generated by today's modern superconducting magnets. In human imaging, most biological tissues are weakly diamagnetic ($\chi < 0$) and oppose the applied field, but oxygen, present in the lungs, sinuses, and other air cavities, is weakly paramagnetic ($\chi > 0$) and strengthens the applied field. This leads to spatially varying B_0 fields within the body, such as the one shown in Figure 2.

Looking at Equation (1), one can see that as the applied magnetic field B_0 increases the internal polarization, M, will also increase. This means that at higher field strengths the amount of off-resonance will increase, and therefore the susceptibility artifacts will be more severe.[34] For an *in vivo* fieldmap at 3 T similar to the 7 T fieldmap shown in Figure 2, as well as the 3 T versus 7 T *in vivo* images with corresponding levels of susceptibility artifacts, we point the reader to Figure 5 of Stockmann and Wald.[35] Due to the scaling with field strength, it is sometimes convenient to describe field susceptibility in terms of ppm, where the typical fieldmap is often less than 1 ppm for most of the brain, but can grow to about 2 ppm at air–brain interfaces.

Magnetic Property	Direction of M Relative to External Field	Relative Magnetic Susceptibility (χ, in ppm)	Example Materials
Diamagnetism	Opposite	-10	Water, most biological tissues
Paramagnetism	Same	+1	Molecular oxygen, O_2
Superparamagnetism	Same	+5000	SPIO contrast agents
Ferromagnetism	Same	>10,000	Iron, steel

FIGURE 1 Magnetic susceptibility. Adapted from https://mriquestions.com/what-is-susceptibility.html[36]
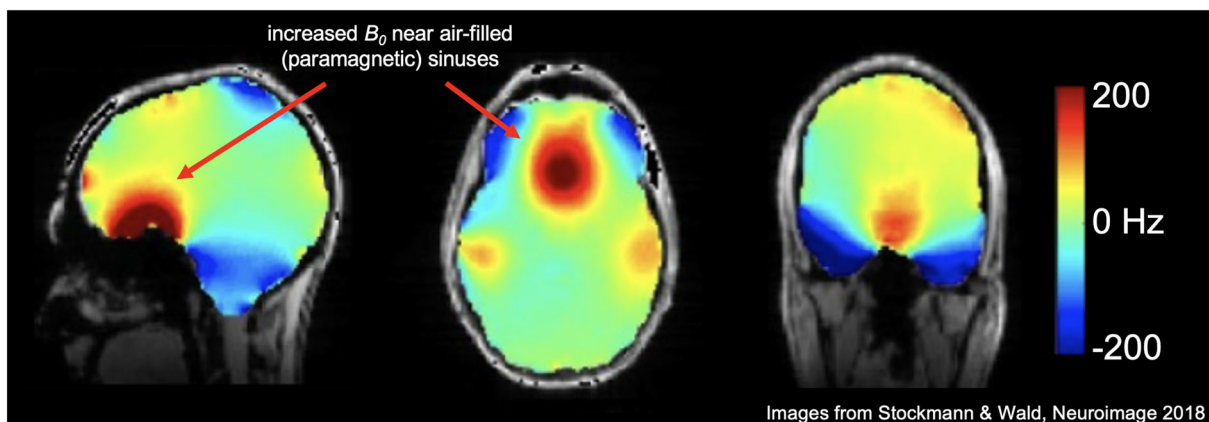

FIGURE 2 B_0 magnetic field in the brain at 7 T with second-order shimming. This fieldmap shows the spatially varying patterns of the B_0 field in the human brain (superimposed over an anatomical image). Even after second-order shimming has been applied to flatten the field, higher-order field inhomogeneities persist. Arrows show that the B_0 field is higher near the air-filled, and therefore paramagnetic, sinuses than in areas in the center of the mostly diamagnetic brain tissue. (Images reused from Stockmann and Wald, 2018[35] with permission.)

2.3 | Chemical shift

Another source of off-resonance is the chemical shift in resonant frequency of different tissues in the body. The most relevant source of chemical shift is from fat, which has a shift in frequency of -3.5 ppm relative to water.[37] At 1.5 T (64 MHz), this corresponds to a shift in frequency of 64 MHz $\times$ -3.5 ppm $= -224$ Hz, and at 3 T a shift of -448 Hz. The earliest accounts of chemical shift image artifacts describe enhanced or diminished borders of organs within the body that have tissue boundaries containing fat.[38,39] This is due to the fat signal shifting within the image because it is off-resonant compared with water (Equation 7). The directions and angles of the slice selection and frequency encoding axes can also affect chemical shift artifacts, leading to them sometimes being present and sometimes not, which can confound diagnosis and affect treatment.[40] Hood et al[37] provide a good review of how chemical shift artifacts impact clinical interpretation of images. The authors also describe what are referred to as chemical shift artifacts of the second kind, which are not shifts in image space of the voxel, but rather a cancellation of the out-of-phase water and fat components in the voxel that leads to a loss of total signal (see Hood et al. Figure 10). These out-of-phase images at a given TE can be compared with images with different TE values where fat is visible, allowing the clear identification of fat.

2.4 | Metal implants

While magnetic susceptibility differences drive many sources of B_0 inhomogeneity as described in Section 2.2, the B_0 effects of metal implants are different, mainly due to the sheer magnitude of the B_0 shifts, leading to effects that often require advanced measures to compensate. Most metal implants in common use today are labeled as MRI conditional, which indicates that MRI scanning is acceptable provided that the specified conditions for safe use are met.[41,42] Allowable or safe use, however, does not mean that the quality of the images is not impacted by susceptibility effects around the implant.

Reference [8] is a review of sources and artifacts due to metal implants as well as a compendium of the various approaches to mitigate the artifacts. Jungmann et al[43] also review mitigation methods and provide numerous imaging examples. As with all susceptibility-induced B_0 changes, these effects scale with field strength. Notably, lower magnetic fields result in smaller distortions and lower-field-strength clinical scanners are often preferred when scanning structures proximal to metal implants, as seen in Figure 3. Further, the lower resonant frequency at lower field reduces the safety and imaging impact of RF (B_1) inhomogeneity around metal implants.

3 | IMPACT ON IMAGING

3.1 | MRI signal equation incorporating off-resonance

In an MRI experiment, the magnetic spins being imaged precess at resonant frequency ω:

$$\omega = \gamma B \tag{2}$$

where γ is a spin's gyromagnetic ratio and B is the magnetic field strength at the spin location. For a proton (^{1}H) in water for which $\gamma/2\pi = 42.577$ MHz/T, at a magnetic field strength $B = 3$ T, the spins precess at roughly 128 MHz. Note that throughout this paper we may use "field" or "frequency" depending on context, but the reader can convert from a precession frequency in hertz to a magnetic field in tesla or vice versa by multiplying or dividing by $\gamma/2\pi$.

To create an image in an ideal MRI experiment, first, the object is placed in a spatially uniform polarizing field, B_0. The ^{1}H spins throughout the entire object will now be precessing at ω_0. Next, spatially varying magnetic fields, G_x, G_y, and G_z, referred to as "gradient fields" or simply "gradients", are applied to linearly change the magnetic field as a function of spatial position, which therefore changes the precession frequency of spins at different locations, i.e., $\omega(x,y,z) = \gamma(B_0 + G_x x + G_y y + G_z z)$. By applying different gradient fields over time, spins at different locations can be encoded, the most common method being Fourier space, or k-space, encoding. The MRI signal as a function of these time-varying gradients can be described using the signal equation:

$$s(t) = \int m(x,y) e^{-i2\pi[k_x(t)x + k_y(t)y]} \, dx \, dy, \quad k_\alpha(t) = \frac{\gamma}{2\pi} \int_0^\tau G_\alpha(\tau) \, d\tau \tag{3}$$

where $s(t)$ is the time-varying MRI signal, $m(x,y)$ is the magnetization at location (x,y), and $k_x(t)$ and $k_y(t)$ are the k-space sampling locations. For brevity, the equation above and the rest of the image encoding mathematics will be in 2D, but it can be extended to 3D as well by adding a third z term to the exponent in Equation (3).
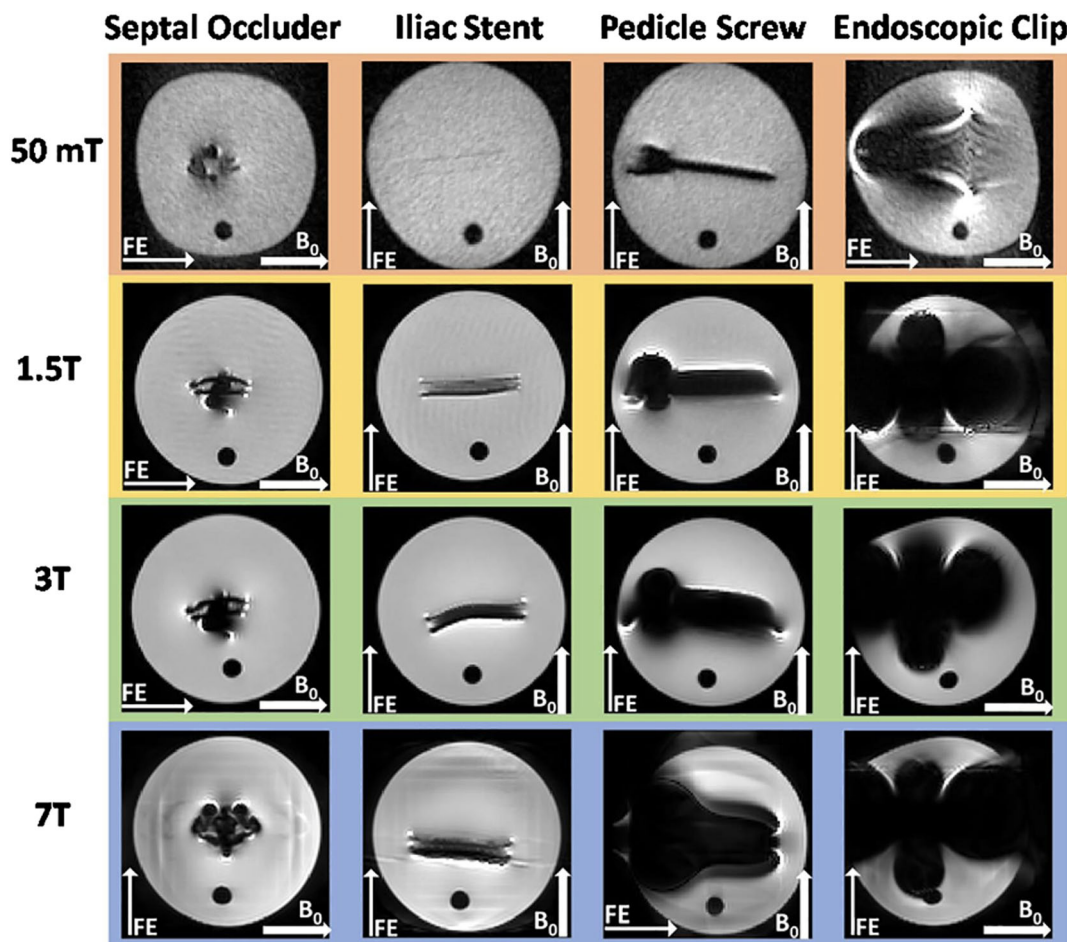
FIGURE 3 Metal artifact from 50 mT to 7 T. Here we show Figure 7 from Van Speybroek et al,[44] where the "worst-case" scenario images for four types of metal implant are demonstrated. (Images reused via open access license.)

By having a spatially uniform polarizing B_0 field, the time-varying signal $s(t)$ is only a function of the applied gradients. However, when B_0 is not spatially uniform, i.e., $B_0(x,y) = B_{0,\text{ideal}} + \Delta B_0(x,y)$, we must add a term to the signal equation for the *additional* (and generally unwanted) spatially dependent phase, $\phi(x,y)$, accrued over time t due to $\Delta B_0(x,y)$:

$$\phi(x,y,t) = \gamma \Delta B_0(x,y)t = \Delta \omega_0(x,y)t = 2\pi \Delta f_0(x,y)t. \tag{4}$$

The phase can now be added to the signal equation using a complex exponential of the product of the fieldmap and the time, t:

$$s(t) = \int m(x,y)e^{-i\Delta\omega_0(x,y)t}e^{-i2\pi[k_x(t)x+k_y(t)y]}\,dxdy. \tag{5}$$

This leads to a breakdown of the encoding properties of the MRI signal equation, since now there will be additional phase in the object that is not a result of the k-space encoding. Depending on the length of the readout, the type of k-space acquisition, and other scan parameters, the excess phase accrued due to off-resonance can lead to various types of artifact such as signal loss, distortions, and blurring.

3.1.1 | Signal loss

When spins in a voxel have different resonant frequencies due to rapid spatial variations in the B_0 field, spins will dephase as seen in Figure 4 (images in Figure 4 were acquired from a healthy subject after obtaining IRB-approved written informed consent). Immediately after RF excitation

(A) Voxel picture of spin dephasing
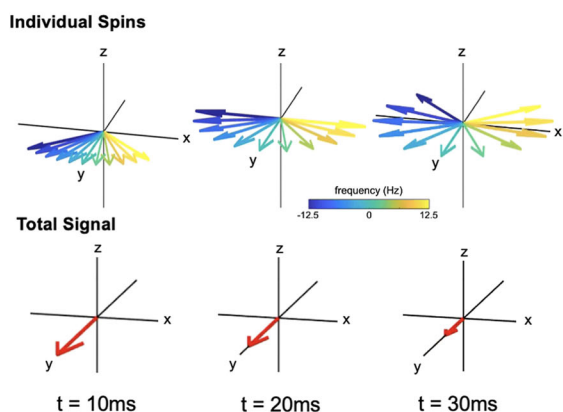
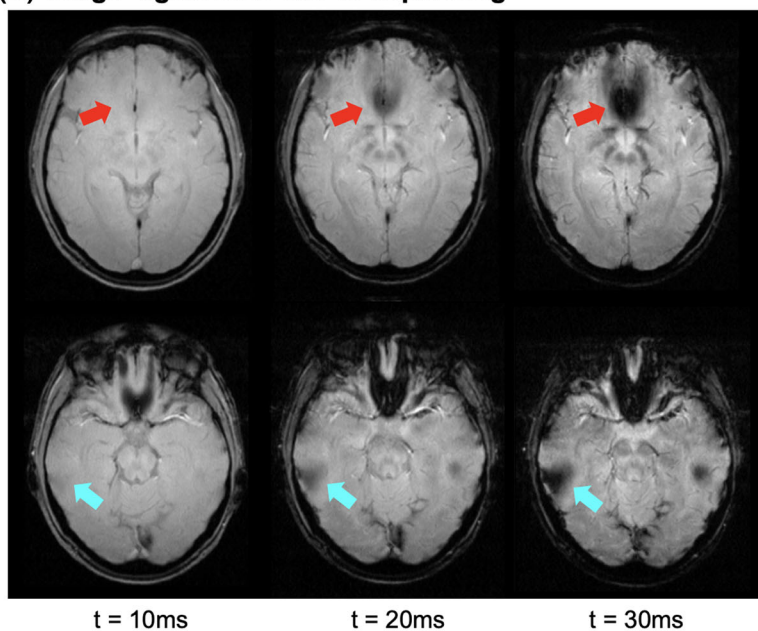## (B) Image signal loss due to dephasing

FIGURE 4 Signal loss from spin dephasing. A, Voxel view of spin dephasing. Spins with different off-resonances will gain different amounts of phase during signal readout leading them to "fan out", and eventually completely cancel each other. B, A gradient echo image is shown for two different slices at three different echo times (TE). At the later echo times, signal loss due to dephasing is present as indicated by the arrows

the spins are all aligned, but during the course of the readout the spins dephase and there is destructive interference in the voxel, referred to as T_2^* decay. The most common way to deal with this signal loss is through the use of spin echoes.[11] In a spin echo sequence, the spins are flipped into the transverse plane, and then after time TE/2 a 180° RF pulse flips the spins about one of the transverse axes. After precessing for time TE/2, the spins will refocus at the echo time, TE. Spin echoes are very robust overall, and because of this spin-echo-based sequences have been the pulse sequence of choice for many of the academic low-field scanners,[20–22,32] as well as the commercially available 64 mT portable brain scanner.[23]

3.1.2 | Image encoding artifacts: distortions and blurring

Spin echoes can mitigate much of the off-resonance based signal loss; however, even using spin echo sequences, significant off-resonance artifacts can be present based on image encoding errors, such as distortion,[45] blurring, and pile-up. Looking at Equation (5), the reduction of intravoxel dephasing by using a spin echo leads to an apparent increase in the $m(x,y)$ term, but the spatial encoding in the exponential of that equation will still be affected by B_0 effects. When there is a non-uniform fieldmap such as the one in Figure 2, there is a breakdown in the encoding since it is not only scanner gradient k-space encoding that is contributing to a voxel's phase, but also phase accrued due to off-resonance. We can factor out 2π and combine the exponentials into one term as follows:

$$s(t) = \int m(x,y) e^{-i2\pi[\Delta f_0(x,y)t + [k_x(t)x + k_y(t)y]]} dxdy. \tag{6}$$

If $[k_x(t)x + k_y(t)y] \gg \Delta f_0(x,y)t$, $s(t)$ will accurately encode the object at $m(x,y)$ for k-space location $(k_x(t),k_y(t))$. However, if there is large off-resonance (or long time t), the phase pattern associated with the encoding will be warped, as seen in Figure 5.

Figure 5 shows the ideal versus the actual encoding pattern, i.e., the phase of the complex exponential in Equation (6), to acquire the sample at $(k_x,k_y) = (0,0.426\,\text{cm}^{-1})$. Note that Figure 5 shows the phase pattern superimposed on the object *for a single point in k-space*, and the encoding error is only a function of the time since RF excitation, t, and the off-resonance fieldmap, $\Delta f_0(x,y)$, not the sampling trajectory used. The specific geometric distortions in image space will be a function of what these encoding errors were *across all k-space points*, and will depend on the sample ordering, with later samples having more excess phase accrued due to off-resonance. As described in more detail below, for Cartesian sequences this encoding error normally manifests in geometric distortions, and for non-Cartesian sequences, such as spiral, this will result in both distortions and blurring.
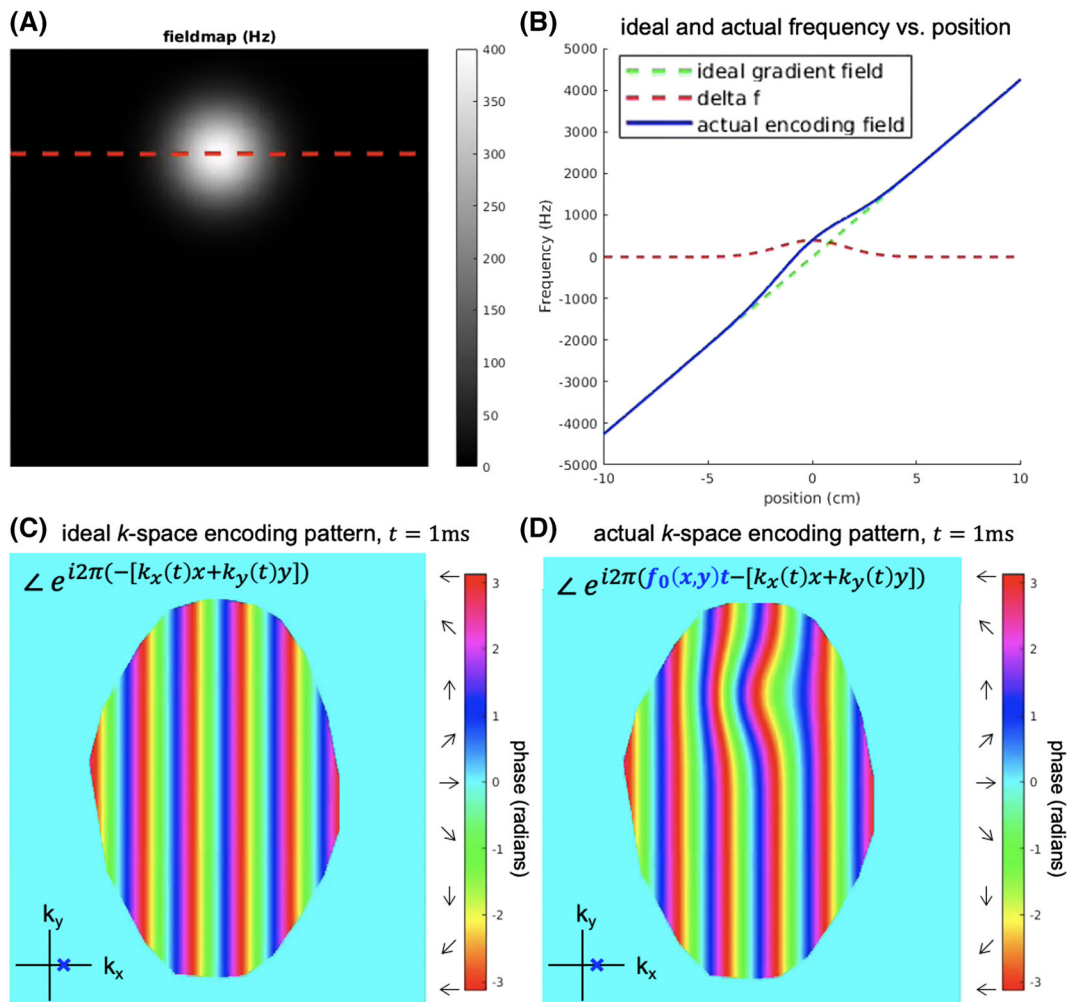
(A)
fieldmap (Hz)

(B) ideal and actual frequency vs. position

- – – ideal gradient field
- – – delta f
- —— actual encoding field

(C) ideal k-space encoding pattern, $t = 1\text{ms}$

$\angle e^{i2\pi(-[k_x(t)x+k_y(t)y])}$

(D) actual k-space encoding pattern, $t = 1\text{ms}$

$\angle e^{i2\pi(f_0(x,y)t-[k_x(t)x+k_y(t)y])}$

FIGURE 5 Ideal versus actual encoding phase at a single k-space location. **A**. Simulated off-resonance fieldmap in Hz. **B**. 1D plots of the encoding fields as a function of position, where the red dotted line correspond to the dotted red line in A. **C**. The ideal k-space encoding phase for $(k_x,k_y) = (0,0.426\text{cm}^{-1})$. **D**. The actual k-space encoding phase for $(k_x,k_y) = (0,0.426\text{cm}^{-1})$. Combined with k-space encoding errors at other k-space sampling locations, this phase error will lead to off-resonance image artifacts

3.2 | Utility of long readouts

In an examination of Equation (4), we can see that off-resonance phase accrual is linearly dependent on the time since excitation. This can be split into two parts: the phase accumulation to the echo time (TE) and phase accumulation during k-space scanning. The first term contributes to signal loss in the $m(x,y)$ term in gradient echo imaging. The second term contributes to k-space distortions and effects, as shown in Figure 5. Thus, long readouts for imaging will show increased distortions. That said, there are advantages to having longer readouts in terms of signal to noise ratio (SNR), k-space scanning efficiency, and overall acquisition speed.

3.2.1 | SNR

For a given repetition time (TR), flip angle, and spatial resolution, the SNR is proportional to the square root of the total acquisition time, $T_{A/D}$,[46] at least to a first approximation. The total acquisition time here is defined as the sum of the length of all acquisitions contributing to a given image. One can also define SNR efficiency as the SNR divided by the square root of overall time to acquire an image. Thus, as one increases the time spent acquiring data in each TR, say by filling in dead times, the SNR efficiency also increases. This is, however, often a minor effect.

3.2.2 | k-space scanning

Perhaps the most important advantage of a long readout is speeding up the image acquisition process, by acquiring more k-space data with each RF excitation. In general, reduced study duration is beneficial for patient comfort and for economic reasons. Beyond this, accelerated imaging is also enabling for many applications. While there are numerous methods to accelerate imaging, notably parallel imaging, k-space scanning with long readouts also plays an important role in reducing scan time. For example, in dynamic imaging applications such as cardiac imaging, there may be advantages to acquiring a larger part of k-space with each excitation so that higher-resolution images can be acquired during a breath hold. In neuroimaging, the ability to "freeze" motion has led to single shot k-space scanning, most commonly using EPI, being the dominant method for acquiring diffusion-weighted and BOLD functional brain images. These are just a few examples where long readout and k-space scanning are useful in MRI.

3.3 | Cartesian imaging: spin-warp and EPI

In Cartesian imaging, data is sampled in straight line segments along k_x. The term "Cartesian" implies that the samples are regularly spaced, though in practice the k_x dimension is sometimes sampled along the trapezoidal gradient ramps (in addition to the plateau) for increased scan efficiency. Since the invention of MRI, Cartesian imaging has remained the "bread and butter" MRI technique despite its relatively low scan-time efficiency compared with non-Cartesian imaging, since (i) it allows fast and simple reconstruction using inverse fast Fourier transforms (iFFTs), (ii) image artifacts due to off-resonance and chemical shift are often easy to recognize and "read through", and (iii) geometric distortions can be corrected using fast and widely available methods.

3.3.1 | Spin-warp imaging

To understand the impact of off-resonance and chemical shift on Cartesian imaging, consider first the case of "spin-warp" imaging, where a single line along k_x is sampled after each RF excitation, with constant gradient amplitude G_x. In this case the k_x-encoding term in Equation (6) can be written as $k_x(t) = \frac{\gamma}{2\pi} G_x t$ and (since the acquisition bandwidth along k_y is effectively infinite) the exponent in Equation (6) becomes $-i2\pi k_x[x + \delta x] - i2\pi k_y(t)y$ where

$$\delta x = \frac{2\pi \Delta f_0(x,y)}{\gamma G_x}. \tag{7}$$

In other words, a voxel at position x with off-resonance frequency $\Delta f_0 \Delta f_0$ will appear at $x + \delta x$ in the reconstructed image. For typical readout bandwidths, δx is negligible for most tissue types at clinical field strengths, but can be on the order of a voxel width, e.g., fat. As a consequence, the acquisition bandwidth for most clinical sequences is kept sufficiently high to avoid significant fat shift. For example, a common acquisition bandwidth is $\pm 32\,\text{kHz}$ (64 kHz total). With the fat chemical shift at 3 T (448 Hz), the corresponding image shift is 1.75 voxels for a 256 readout sample. Note that Equation (7) ignores any B_0 inhomogeneity *within* the voxel centered at location (x,y), and hence does not describe any signal loss that may occur at a given echo time (TE).

3.3.2 | EPI

In EPI, multiple lines at different k_y-encoding levels are acquired after RF excitation. This is done by playing a small y-gradient trapezoid "blip" after the end of each k_x line, and then traversing the subsequent line in reverse direction (non-flyback EPI). Assuming regular sampling along k_y with subsequent "echoes" spaced τ_s apart in time, and ignoring the (typically small) shift δx along the frequency-encoding direction, the exponent in Equation (6) becomes $-i2\pi k_x x - i2\pi k_y[y + \delta y]$, where

$$\delta y = \frac{2\pi \Delta f_0(x,y)}{\gamma \overline{G_y}} \tag{8}$$

is the spatial shift (along y) in the reconstructed image. Here, $\overline{G_y}$ is the *average* gradient amplitude of the y blip over the echo time spacing τ_s, which is much smaller than the readout gradient amplitude G_x in Equation (7). As a result, EPI can produce substantial spatial shifts along the phase encoding (PE) direction, here k_y. However if the user were to change the PE direction, the spatial shifts would also change direction, as

these off-resonance induced spatial shifts are primarily in the PE direction. A useful way to think about these EPI distortions is to express the average gradient in the PE direction in units of Hz/cm, as follows:

$$\overline{G}_{y,\text{Hz/cm}} = \frac{\gamma \overline{G_y}}{2\pi} = 1/(\tau_s \, \text{FOV}/R) \tag{9}$$

where τ_s = echo spacing and R = in-plane acceleration. Typical values are about 66 Hz/cm for high-resolution fMRI (2 mm isotropic resolution, τ_s = 0.75 ms, FOV = 20 cm, $R = 1$), 100 Hz/cm for low-resolution fMRI (τ_s = 0.50 ms, FOV = 20 cm, $R = 1$), and about 133 Hz/cm for diffusion tensor imaging (DTI) with 2 mm resolution and in-plane acceleration (τ_s = 0.75 ms, FOV = 20 cm, $R = 2$). The spatial shift along the PE direction (Equation 8) is then found by dividing the local off-resonance Δf_0 by the average gradient expressed in Hz/cm.

3.3.3 | Interleaved and readout mosaic segmented EPI

EPI comes in several multishot variants that make various tradeoffs between image artifacts and scan efficiency. In addition to geometric distortions as just described, another consideration is T_2^* decay during the echo train, which acts as a k-space filter resulting in blurring in image space.

In interleaved EPI, the area of each k_y-encoding blip, and hence $\overline{G_y}$, is increased, making each EPI train undersampled by a factor equal to the number of segments (shots) N_s. This reduces the geometric shifts, and the time allowing for T_2^* decay, by this same factor N_s. Interleaved EPI is typically implemented by shifting the start of subsequent EPI segments by a time n/τ_s, where $n = 0,...,N_s - 1$ is the shot number, to avoid abrupt phase jumps in k_y-space due to off-resonance. A potential drawback of interleaved EPI is shot-to-shot variability in the acquired data, resulting from, e.g., physiological fluctuations or subject motion.

An alternative scheme useful for diffusion MRI is readout mosaic segmented EPI, where only a portion ("blind") of k_x-space is acquired during each shot, while sampling all desired k_y locations per shot.[47,48] The advantage of this approach is that it preserves the regular sampling along k_y in the presence of shot-to-shot k-space shifts due to rotational motion in the presence of diffusion-encoding gradients.[49] By introducing a small overlap between blinds along k_x, such shifts need not introduce any gaps along k_x as well. A drawback of this approach is that the echo time spacing is not reduced by the full segmentation factor N_s due to finite gradient rise time, and hence the reduction in geometric shift is somewhat smaller than for interleaved EPI for a given N_s.

3.4 | Non-Cartesian acquisitions

While much of MRI carried out on clinical scanners uses Cartesian acquisitions such as spin-warp or EPI, there are numerous useful applications that use non-Cartesian acquisitions. This is a broad class of image acquisitions that typically do not acquire data along parallel lines in k-space. Some aspects are similar to Cartesian imaging, for example, the need to acquire data over a prescribed area in k-space for the desired spatial resolution and to acquire k-space data with sufficient sample density to prevent aliasing. The nature of the off-resonance artifacts, however, is quite different. Below, we discuss these effects for radial line and spiral imaging, but note that there are yet other non-Cartesian trajectories, e.g., rosettes,[50] that have quite complicated off-resonance behavior that is beyond the scope of this review.

3.4.1 | Radial line and spiral imaging

Radial line and spiral imaging are useful in a number of applications. For example, radial line acquisitions in 2D or 3D have substantial utility in zero- and ultra-short-TE (ZTE and UTE) imaging,[51,52] angiography,[53] and contrast enhanced abdominal imaging.[54] Spiral imaging has been shown to be useful in fMRI,[55] cardiac imaging,[56] and brain imaging.[57]

Spiral and radial line imaging have off-resonance features that are similar to each other, but are quite different from spin-warp and EPI. For each line of a radial line acquisition, there is a shift in the radial direction in the form

$$\delta r \equiv \frac{2\pi \Delta f_0(x,y)}{\gamma G_r} \tag{10}$$

where G_r is the strength of the radial gradient. Since the direction of the radial gradient is constantly changing and ultimately points in all directions, the net effect is not a single shift, but a shift in all directions. More specifically, any off-resonant point in the object maps to a ring-like response of radius δr. This is equivalent to saying that the point spread function (PSF) or impulse response is this ring-like function, the radius of which, δr, is proportional to the off-resonance frequency, $\Delta f_0(x,y)$. For a complex image, this manifests as a blur of radius δr.

For spirals, the off-resonance response is again a radial shift in all directions, with amplitude

$$\delta r_s \approx \frac{2\pi \Delta f_0(x,y)}{\gamma \overline{G_r}} \tag{11}$$

where $\overline{G_r}$ is the average outward component of the spiral gradients. One can also infer the average outward component with $\overline{G_r} = 2\pi k_{max}/T$, where T is the length of the spiral readout. Now, any off-resonant point in the object maps to a ring-like response of radius δr_s, and as with radial imaging this is proportional to the off-resonance frequency, $\Delta f_0(x,y)$. As can be seen from the alternate $\overline{G_r}$ expression, the blur is also proportional to the length of the spiral readout, T. Again, for a complex image, this manifests as a blur of radius δr_s. For spiral imaging, the relationship that the blur is a ring of radius δr_s is only approximate because the average outward component typically varies during the readout, making the actual blur function a bit more complicated. Still, the main principle is that longer readouts make the off-resonance image blurring worse.

The off-resonance behavior also extends to three dimensions. For examples, ZTE imaging and angiography applications often use a 3D radial line acquisition. While spirals do not extend directly to 3D, there are 3D trajectories such as 3D cones, trajectories that spiral outward while rotating along two axes (sometimes called yarn trajectories), and spiral-radial hybrids[58] that have off-resonance properties similar to spirals. In these cases, we consider induced blur to be occurring in all three dimensions, that is, the PSF or impulse response is an annular sphere with radius δr (or δr_s). Again, greater off-resonance and longer readouts increase the radius of the blurring function.

The ways in which off-resonance affects EPI and spiral images at 3 T is shown in Figure 6 (images in Figure 6 were acquired from a healthy subject after obtaining IRB-approved written informed consent). As expected the artifacts in the spiral image are primarily blurring, and the artifacts in the simulated EPI image are primarily geometric distortions along the phase encode (vertical) direction. Additional details of the simulation can be found at https://github.com/fmrilab/B0-review-2022.

3.5 | Imaging near metal implants

Though not ferromagnetic, the susceptibility differences between metals and tissues are substantially larger than the differences between tissues and the surrounding air. These large susceptibility differences, in combination with the often large mass of these implants, lead to similar, but magnified, B_0 effects. For example, much of gradient echo (GRE) imaging is infeasible in close proximity to implants, except for the very shortest TE times, meaning that most studies use spin echo (SE) or fast/turbo spin echo (FSE/TSE) acquisitions. Similarly, rapid imaging methods such as EPI or spiral imaging with implants will typically produce artifacts that are too severe to correct. There are often severe geometric distortions in the readout (frequency encoding) direction associated with implants, including signal voids and piling up artifacts. Another common issue is the distortion of the slice profiles, where there can be spatial displacement several slice thicknesses in magnitude, distorted slice profiles such as potato chips, and variable slice thicknesses. In both frequency encode and slice effects, the spatial distortions are proportional to the frequency offset divided by the bandwidth per pixel (or slice thickness).
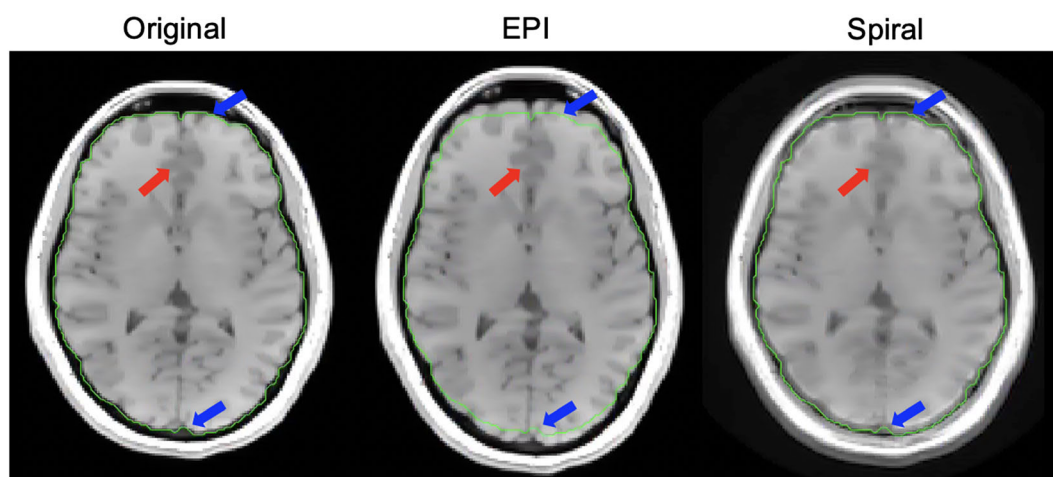

FIGURE 6 Image simulations: Cartesian versus non-Cartesian. Here we show the different off-resonance effects from EPI versus spiral acquisition. In the EPI image, geometric distortion of the brain is visible with a distortion sensitivity of 75 Hz/cm (see Equation 9), a typical value, resulting in the brain being stretched compared with the original Cartesian spin-warp image (blue arrows). In the spiral image, there is a large amount of blurring, noted by the red arrow, but there is less geometric distortion than in EPI

4 | ESTIMATING B_0 FIELD INHOMOGENEITY

4.1 | MRI sequences for acquiring fieldmaps

Before correction for B_0 inhomogeneity artifacts, it is often necessary to acquire and estimate the fieldmap. The simplest way to estimate a B_0 fieldmap is to create a pulse sequence that acquires two sequential gradient echo images at different TE times, and then subtract their relative phases to obtain the amount of precession at that voxel over the echo time difference ΔTE. The phase difference is then scaled by ΔTE to obtain the fieldmap:

$$\Delta\phi(x,y) = \angle m(x,y,TE_1) - \angle m(x,y,TE_2) \tag{12}$$

$$\Delta\omega_0(x,y) = \frac{\Delta\phi(x,y)}{\Delta TE}. \tag{13}$$

This is the basic idea behind B_0 fieldmapping in MRI, but there are many ways to estimate a fieldmap within this general approach. The choice of ΔTE will affect the quality of the fieldmaps, and has been quantitatively evaluated in prior work.[59] Normally gradient echo images at short TE times are used to avoid distortions in the underlying fieldmap, but for applications using EPI there has also been work in using EPI-based fieldmaps.[60] While EPI fieldmaps will be distorted given the longer TE times required, they have the advantage that they will be distorted in the same way and also experience the same eddy currents as the EPI data used in the imaging experiment, potentially allowing for easier look-up of the off-resonance at any voxel.

Another consideration when calculating fieldmaps is phase wrap. A longer ΔTE is desirable because it will increase the SNR of the phase difference measurement. However, when ΔTE is increased, more phase wrap can occur. Fortunately, many tools such as FSL[61] include phase unwrapping algorithms that are useful when calculating off-resonance field maps, such as the automated method introduced by Jenkinson in 2003.[62]

There have also been recent approaches to rapidly acquire B_0 fieldmaps along with transmit coil patterns (B_1^+), receive coil sensitivity (B_1^-), and eddy current maps in as little as 11 s at $1 \times 2 \times 2\text{mm}^3$ resolution at 3 T.[63] This kind of approach is especially useful for model-based image reconstructions that incorporate B_0 (see Section 5.4), since B_1^- maps are often needed as well.

There are requirements that the fieldmaps be reasonably accurate and not too noisy. As a general rule, the error/noise level should be below the level of observable degradation of the PSF. One rule of thumb is for the error and noise levels to be below 0.25 cycle of phase over the read-out. For example, if you want to correct the field effects for a 25 ms readout, 40 Hz offset will produce one cycle of phase over the readout and thus we would want worst case errors to be below 10 Hz. Often, the fieldmaps are smoothly varying except for small air/tissue boundaries. As such, it is often expedient to collect fieldmaps at lower spatial resolution (2–3 mm) than the images to be corrected (1–2 mm).

4.2 | Hardware methods

In addition to measuring a fieldmap using a sequence, it is possible to employ external hardware and/or built-in scanner hardware to monitor changes in off-resonance. Generally these types of hardware tracking method will be used for dynamic B_0 correction (see Section 5.5) after an initial B_0 map has been measured using a fieldmapping sequence. One option is to use NMR field probes,[64–66] which measure the changes in phase of the MRI signal within small external samples. These probes are now commercially available (https://skope.swiss/) and have been used in applications such as diffusion MRI, fMRI, and ultra-high-field imaging. Another approach is to use free induction decay (FID) measurements from a multicoil receive array, which can encode changes in signal based on the different spatial locations of the coils. By combining with a reference image from each coil, Wallace et al. showed that FIDs can be used to dynamically track up to second-order field changes.[67]

4.3 | Optimization and smoothing methods

After multi-TE data has been acquired, Equation (13) is the simplest way to calculate a fieldmap, but the maps are often improved by using some form of smoothing or regularization due to the difficulty of obtaining B_0 values near the edges of the anatomy. In the original TOPUP paper,[68] a smoothed version of the fieldmap that is based on polynomial fitting was used. The work by Hutton et al,[59] in addition to examining ΔTE, also quantitatively evaluates how the amount of smoothing used affects fieldmap estimates.

There are also optimization-based approaches that use a multiterm objective function, where the phase differences between multiple TE values is a data fit term and another regularization term penalizes rapidly varying and sudden field changes.[69] This method has been expanded to

incorporate a more efficient optimization algorithm and the ability to input multicoil data.[70] Additionally, it is possible to jointly optimize for a fieldmap and an image, and these approaches are described in Section 5.4 on model-based image reconstruction.

5 | CORRECTION STRATEGIES

In this section we discuss strategies to correct for off-resonance artifacts in MRI. Many of the methods described could fit into multiple categories, but we have broadly categorized them to help in describing the different options available to MRI users, as outlined in Figure 7.

5.1 | Artifact prevention and reduction

5.1.1 | Hardware-based artifact mitigation

The most straightforward way to prevent B_0 artifacts is to have as uniform a field as possible before starting a scan, and the process of refining the uniformity of the B_0 field is referred to as *shimming*.[72] Shimming can be done either by improving the static B_0 field hardware (i.e., with superconducting shim magnets or ferrous passive elements) or by actively changing the currents in the scanner's electro-shim coils, which include the gradient coils. An example of passive shimming at low field is the work of Liu et al., where on their 50 mT scanner they originally had a 2000 ppm peak-to-peak uniformity over a 24 cm diameter spherical volume (DSV) within their SmCo dipole magnet, but after adding smaller passive shim magnets their uniformity was increased to 250 ppm.[20] Automated shimming is a standard part of a clinical MRI pre-scan calibration (at least for the constant linear shim terms) and for most users this will be automatic, but for certain types of acquisition, such as MRS that requires a very uniform field,[73] the user may need to carry out manual shimming as well.

In addition to shimming, using a lower magnetic field is a direct way to reduce B_0 artifacts. As was discussed in Section 2, B_0 field changes that are attributable to susceptibility and chemical shift scale with field strength, so these artifacts are generally worse at higher field. There are some B_0 artifact mitigation strategies that are harder at low field due to decreased SNR, but in general going to lower field will reduce signal loss and encoding artifacts from an inhomogeneous field.

5.1.2 | Sequence-based artifact mitigation

When designing an MRI sequence, parameters can be adjusted to reduce the effects of off-resonance. Using a short readout time (high acquisition bandwidth) will limit the amount of extra phase accrued due to off-resonance and therefore reduce artifacts. The use of parallel imaging techniques[13,74] is an effective way to reduce the readout length of a single-shot acquisition (such as EPI or single-shot spiral), by allowing the user to collect less k-space data each shot. If using longer readouts, spin echoes and spin echo trains will refocus spins and avoid much of the T_2^* signal loss.[11,12] Chemical shift artifacts can be avoided by using a short-time inversion recovery (STIR) sequence that nulls recovering fat signal, inserting fat saturation modules before water excitation (an RF excitation at the fat frequency and then a large crusher gradient), or by using a spectrally selective RF pulse centered around the water resonant frequency.[75] Further, while this generally has the downside of longer scan time due to

Artifact Prevention (Section 5.1)	**B_0 Correction Methods (Sections 5.2-5.6)**
- Hardware based - passive & active shimming - lower-field MRI - Sequence based - spin echoes - shorter readouts: parallel imaging, multishot imaging - fat suppression / nulling (STIR) - smaller voxels: parallel imaging, simultaneous multislice	- EPI/Cartesian focused - Image Space: TOPUP - PSF - Non-Cartesian focused - Direct/Analytical: conjugate phase, SPHERE - Autofocusing - Model based image reconstruction including B_0 - Dynamic corrections - Corrections for larger B_0 shifts around metal implants - View angle tilting - MAVRIC - SEMAC

FIGURE 7   Common B_0 artifact mitigation strategies

additional encoding, using smaller voxels will decrease the possible signal loss due to a more local neighborhood of spins being averaged in each voxel. Parallel imaging and simultaneous multislice imaging[14] are effective strategies to reduce voxel size without increasing scan time.

5.2 | EPI

Several methods for correcting geometric and intensity distortions in EPI have been proposed (see, e.g., References [76,77] for recent overviews), and here we focus on three of the more popular ones: image-based correction using an acquired B_0 map, image-based correction using two reference scans with opposite phase-encode blip directions, and the PSF mapping approach. These have all proven to be useful for EPI distortion correction in fMRI and diffusion imaging.

5.2.1 | Fieldmap-based correction

One popular approach is based on the separate acquisition of an undistorted B_0 map (e.g., using spin-warp 3D GRE), that is used to calculate the shift δy (Equation 8) for each spatial location.[68] The pixel values in the reconstructed (distorted) image are then shifted along the phase-encode direction by $-\delta y$. This is followed by an intensity correction step based on the spatial gradient of δy.[68] Potential drawbacks of this approach include inaccurate correction near object edges due to inaccurate B_0 estimates (partial-volume effects), and inability to resolve overlapping pixels.

5.2.2 | Opposite phase-encoding scans

Another widely used approach that also operates on magnitude images is TOPUP (Figure 8),[71] that uses as input two EPI images that differ only in the sign of the phase-encoding blips (i.e., traversing k_y in the positive and negative, or bottom-up and top-down, directions). The TOPUP model is

$$\begin{bmatrix}\mathbf{f}_{+,i}\\\mathbf{f}_{-,i}\end{bmatrix}=\begin{bmatrix}\mathbf{K}_{+,i}\\\mathbf{K}_{-,i}\end{bmatrix}\mathbf{x}_i \tag{14}$$

where $\mathbf{x}_i$ is the ith column (along y) of the undistorted true image $\mathbf{x}$, $\mathbf{f}_+$ and $\mathbf{f}_-$ are the distorted bottom-up and top-down images, respectively, and $\mathbf{K}_{+,i}$ and $\mathbf{K}_{-,i}$ are real-valued square matrices that map the pixel locations in the true image column $\mathbf{x}_i$ to the observed image columns $\mathbf{f}_{+/-,i}$. In the absence of B_0 inhomogeneity, $\mathbf{K}_{+,i}$ and $\mathbf{K}_{-,i}$ would be the identity matrix $\mathbf{I}$.

With knowledge of B_0 (which determines $\mathbf{K}_{+,i}$ and $\mathbf{K}_{-,i}$), Equation (14) can be inverted to obtain a least-squares estimate $\hat{\mathbf{x}}$ of the true image, with the benefit that pixels that overlap in one of the images (causing either $\mathbf{K}_{+,i}$ or $\mathbf{K}_{-,i}$ to be singular) are separated in the other, which enables the underlying true image to be resolved.

In the absence of B_0 inhomogeneity, $\hat{\mathbf{x}}_i$ is simply the average of $\mathbf{f}_{+,i}$ and $\mathbf{f}_{-,i}$. Furthermore, the TOPUP model can be used to estimate B_0 from the two EPI scans (obviating the need for a separately acquired B_0 map), by enforcing consistency between the observed images $\mathbf{f}_{+,-}$ and the predicted images $\hat{\mathbf{f}}_{+,-}$ created by distorting $\hat{\mathbf{x}}$ using Equation (14):

$$\widehat{\mathbf{b}_i}=\arg\min_{\mathbf{b}_i}\left|\begin{bmatrix}\mathbf{f}_{+,i}\\\mathbf{f}_{-,i}\end{bmatrix}-\begin{bmatrix}\mathbf{K}_{+,i}(\mathbf{b}_i)\\\mathbf{K}_{-,i}(\mathbf{b}_i)\end{bmatrix}\hat{\mathbf{x}}_i(\mathbf{b}_i)\right|_2^2 \tag{15}$$

where $\mathbf{b}_i$ parametrizes the displacements (using the notation from[71]), and we have made the dependence of $\hat{\mathbf{x}}_i$ on $\mathbf{b}_i$ explicit. Knowledge of $\mathbf{b}_i$ yields an estimate of the fieldmap B_0, which can then be used to create an undistorted image using the approach described above. Advantages of this approach include estimation of δy (Equation 8) from fast EPI scans, and avoiding potential inaccuracy issues in the directly acquired B_0 maps. However, like fieldmap-based correction, TOPUP cannot easily correct for signal pile-up in regions with severe B_0 inhomogeneity. While there are some limits to how much correction is possible, this approach has the important practical advantage that it can operate on magnitude images after simultaneous multislice reconstruction and coil combination.

5.2.3 | PSF mapping

Another way to obtain $\delta y(\mathbf{r})$ is based on measuring the PSF along y.[78–80] This can be done by performing a calibration prescan wherein one adds an additional k_y encoding blip prior to the EPI readout, and repeats the measurement with different blip areas. For a 2D EPI acquisition, this
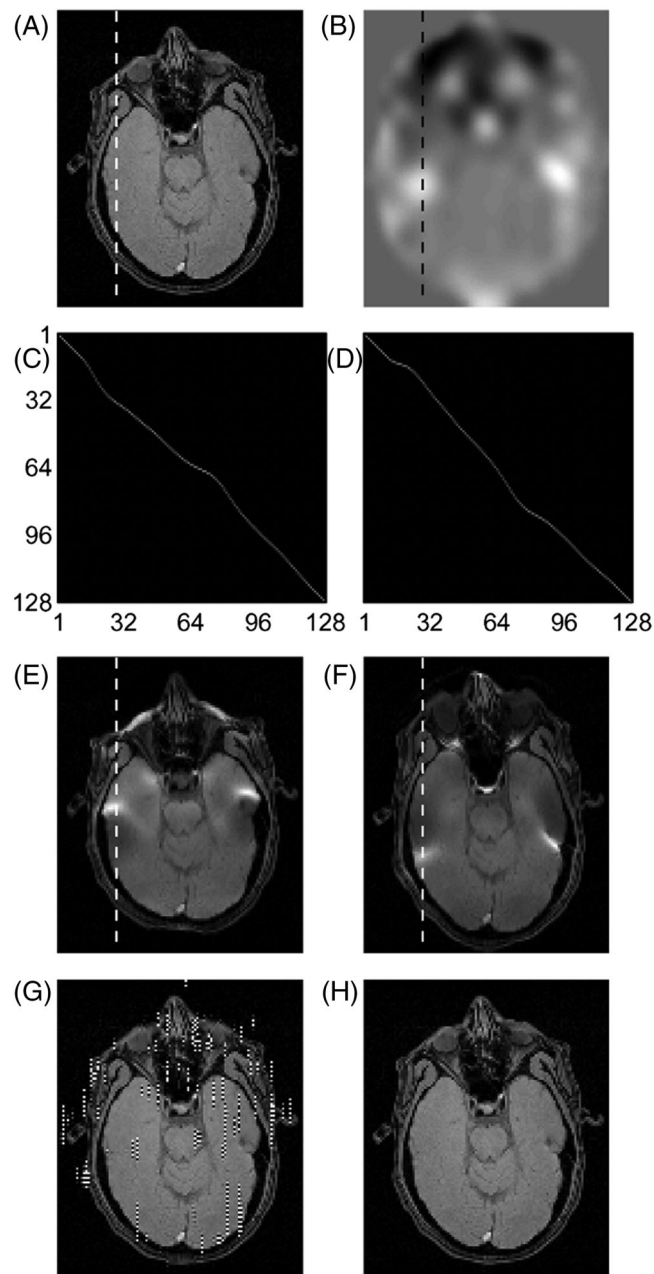
Andersson, et al., Neuroimage, 2003

FIGURE 8 Illustration of EPI distortion correction using Equation (14). A, Ground-truth (undistorted) object; B, fieldmap. C, D, $K_{+,i}$ and $K_{-,i}$ for the dashed lines in E, F. E, F, Distorted images f_+ and f_-. G, Distortion correction attempt using only f_+. H, Successful distortion correction using Equation (14). (Images reused from Andersson et al., 2003[71] with permission.)

additional "constant-time" encoding yields a 3D dataset where the spatial profile in the constant-time encoding dimension is the PSF.[78] The pixel shift can then be obtained as the center (peak) of the PSF.[80] An advantage of this approach is that the shift is estimated with the same EPI read-out as the imaging sequence to be corrected, and hence experiences and accounts for the same eddy currents and concomitant gradients.

5.3 | Non-Cartesian

Off-resonance effects lead to blurring and other distortions for non-Cartesian acquisitions, and this is often more objectionable than the geometric distortions seen in Cartesian imaging. Thus, it is often necessary to make some sort of off-resonance correction in order to produce clinically useful images. This section describes common approaches for this correction that are applicable to radial line, spiral, and related *k*-space trajectories.

5.3.1 | Direct/analytical methods

Conjugate phase (CP) reconstruction

In the absence of off-resonance, the signal equation in Equation (6) can be seen as a simple Fourier transform and a good image reconstruction will be simply an iFFT. For a non-Cartesian acquisition, one can implement an approximate iFFT as

$$\hat{m}(x,y) = \frac{1}{M}\sum_i w_i y_i e^{i2\pi(k_{x,i}x + k_{y,i}y)} \approx F^{-1}\{y(t)\} \tag{16}$$

where i is the index over M k-space samples $y_i = y(t_i)$ at k-space locations $(k_{x,i}, k_{y,i})$, and w_i is the sample density compensation term that accounts for uneven distribution of k-space samples common in non-Cartesian methods. In practice, this expression is commonly implemented by some sort of interpolation in the k-domain to a Cartesian grid (known as gridding) followed by iFFT operators or by using integrated functions such as the NUFFT.[81]

When considering off-resonance effects, a good image reconstruction may be to compensate for the off-resonance phase accumulation in the image reconstruction at every time point and for each location (x,y)[82,83] as shown here:

$$\hat{m}(x,y) = \frac{1}{N}\sum_i w_i y_i e^{i2\pi(\Delta f_0(x,y)t_i + k_{x,i}x + k_{y,i}y)} \tag{17}$$

where the $\Delta f_0(x,y)t_i$ term is known as the CP correction for the off-resonance (see Figure 9 for an image example).

There are limitations to the CP reconstruction, notably in that it is not a true inverse, but rather an approximation.

In particular, this approach fails to give high-quality image reconstructions when the magnetic field ($\Delta f_0(x,y)$) varies rapidly in space and therefore the ring-like PSF will also vary rapidly in space. If two PSFs overlap in space and these PSF functions are different, then this approach cannot fully correct for both blurring functions. An alternate way to think about this is that rapidly varying Δf_0 corresponds to a local gradient, and therefore the k-space is distorted for locations with large local gradients.[85] The distorted local k-space limits the effectiveness of the CP reconstruction. Model-based image reconstruction, described below, is more robust to address rapid variations in the field map.

Efficient approximations

While Equation (16) has fast implementations with gridding or the NUFFT, Equation (17) is no longer an inverse Fourier transform due to the $\Delta f_0(x,y)t$ term. Still, there are computationally efficient implementations that result from decomposing this term into a sum of terms that vary only in space and terms that vary only in time. The exponential can be modeled as a summation of basis functions[86,87]:

$$e^{i2\pi\Delta f_0(x,y)t} \approx \sum_{l=1}^{L} b_l(t)c_l(x,y) \tag{18}$$

where b_l and c_l represent the basis functions for the time and image space, respectively. Note that frequency, $\Delta f_0(x,y)$, varies only with space.

The first such implementation was the so-called time-segmented approximation[88] to the CP correction term, where $b_l = b_l(t - \bar{t}_l)$ is a family of time-varying weighting functions centered at $\bar{t}_l$ and $c_l = e^{i2\pi\Delta f_0(x,y)\bar{t}_l}$ is a spatially varying phase function corresponding to $\bar{t}_l$. This approximation to Equation (17) is

$$\hat{m}(x,y) \approx \sum_{l=1}^{L} F^{-1}\{b_l(t - \bar{t}_l)y(t)\} e^{i2\pi\Delta f_0(x,y)\bar{t}_l} \tag{19}$$

where F^{-1} is the gridding or NUFFT inverse transform of windowed segments of $y(t)$. A related form is known as the multifrequency interpolation (MFI) method,[89,90] which modulates the acquired data at frequencies f_l using $b_l = e^{i2\pi f_l t}$ and interpolates between modulated images using $c_l(x,y)$. This approximation to the CP reconstruction is

$$\hat{m}(x,y) \approx \sum_{l=1}^{L} F^{-1}\{e^{-i2\pi f_l t}y(t)\} c_l(\Delta f_0(x,y) - f_l). \tag{20}$$

Observe that L Fourier transforms are implemented in both of these approximations, so while they are about L times slower than Equation (16) they are still substantially faster than the discrete Fourier transform implementation of Equation (17).

The time-segmented approximation and the MFI methods perform similarly and can be viewed as low-rank approximations to the $e^{i2\pi\Delta f_0(x,y)t}$ term. The interpolation functions can be selected optimally according to different optimality criteria.[86,90]
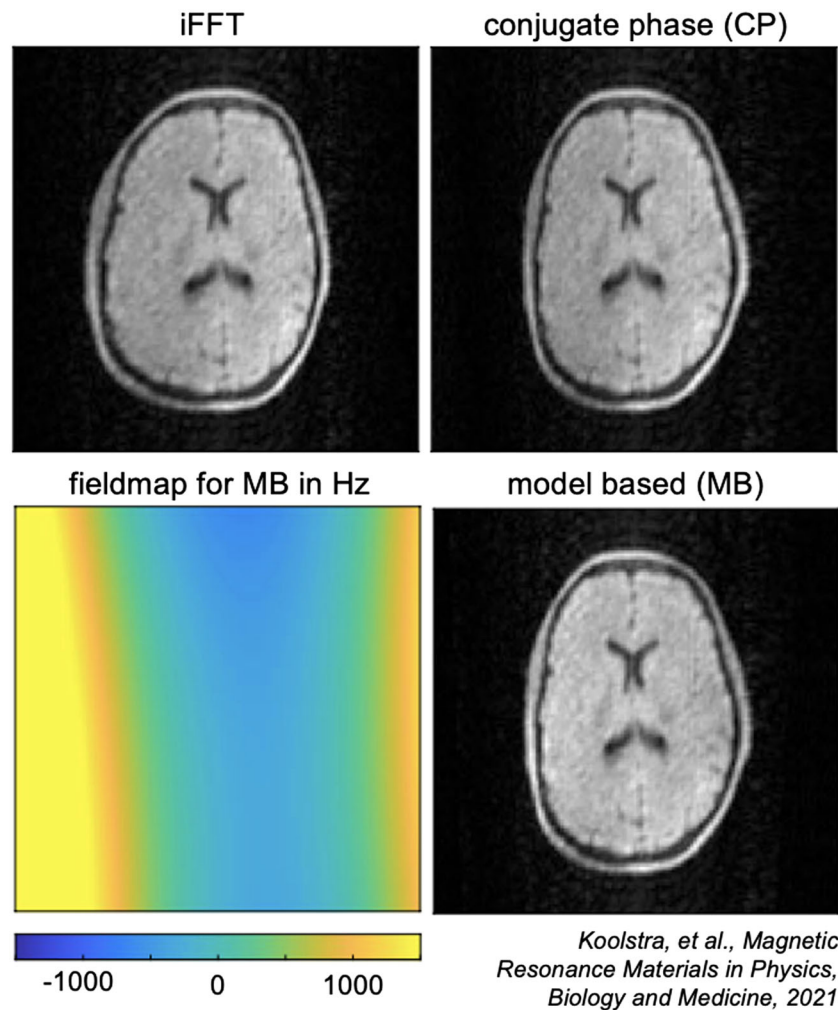
FIGURE 9 CP and MB reconstruction at 50 mT. Compared with a standard iFFT reconstruction, CP and MB reconstructions both correct for geometric distortions due to off-resonance, especially in the right side of the brain where the magnetic field off-resonance is stronger. MB also shows more uniform signal intensity. (Images reused from Koolstra et al., 2021[84] via open access license.)

Deblurring with deconvolution

While the above approaches implement off-resonance correction as part of the image reconstruction, this can also be implemented in the image domain using deconvolution.[91] Provided the spatial extent of the PSF or blurring function is small, one can deblur the images using a space variant deconvolution, where the deconvolution kernel is guided by the acquired fieldmap. Ahunbay et al[91] showed that in some circumstances the deconvolution kernel is separable into x and y, which can greatly reduce the computational burden.

Simulated phase evolution rewinding (SPHERE)

An alternate approach to field correction that is similar to the CP approach is to apply the CP correction to the forward Fourier transform rather than the inverse transform. This general approach is known as SPHERE.[92] The approach starts with a reconstruction (iFFT) that does not apply an off-resonance phase correction, e.g., Equation (16), and follows it with a forward transform back to the k-domain; however, during the forward Fourier transform, the CP correction is applied:

$$y_{\text{corr}}(t) = \sum_{x,y} \hat{m}(x,y) e^{-i2\pi(\Delta f_0(x,y)t + [k_x(t)x + k_y(t)y])} \tag{21}$$

where the sign of the complex exponent $-\Delta f_0(x,y)$ is the opposite of that in the signal equation, Equation (6), thus applying the CP to compensate for the off-resonance phase accumulation. This is followed by a simple iFFT to produce the final image. As with the CP reconstruction, the $\Delta f_0(x,y)t$ term means that the forward transform is no longer a Fourier transform, but the time-segmented approximations and the MFI can be used to implement this in a computationally efficient manner. Schomberg's review[93] provides a detailed mathematical analysis of CP and SPHERE methods, along with fast implementation strategies and timing comparisons of the different approaches.

5.3.2 | Autofocusing

One unique aspect of non-Cartesian imaging is that the PSF may allow for autodetection of off-resonance based on features of the image. Conceptually, it is like an autofocus camera where different parts of the image have different off-resonance corrections to produce a fully deblurred image. This is done by examining image features rather than through the use of a fieldmap. In Reference,[94] a multifrequency reconstruction was used, in which non-Cartesian images were reconstructed to produce a family of images where different parts of each image are unblurred. An image metric based on a measure of how closely the phase of low-spatial-frequency images aligned with the phase of high spatial frequencies was used to determine, for each voxel (x,y), which modulated image was sharpest. This measure works well for spiral imaging because the low spatial frequencies are acquired earlier than high spatial frequencies, and off-resonance will lead to these components being out of phase. In recent work,[95] real time speech MRI with spiral readouts was automatically deblurred using a sharpness metric of features in the vocal tract. Interestingly, these autofocus methods can produce a fieldmap based on the selected image.

Machine learning

One challenge to autofocusing is the selection of an appropriate measure of image sharpness. Because of the predictable and reproducible nature of the off-resonance effects in non-Cartesian imaging, it is possible to train a neural network to learn and remove image blurs. In Reference [96], body imaging with 3D cones trajectories and long readouts was deblurred by a convolutional neural network (CNN) that directly maps blurred images to unblurred images acquired with shorter readouts (but an overall longer scan time). This type of approach has also been applied to speech MRI, where a longer-readout image was deblurred using a CNN, allowing for longer k-space readouts and therefore higher temporal visualization of speech in the hard-to-correct areas around the mouth and sinuses.[97] In another approach, a CNN is trained to estimate the fieldmap directly, and then uses the fieldmap within a model-based image reconstruction to produce unblurred images.[98]

5.4 | Model-based image reconstruction incorporating B_0

As the use of techniques such as parallel imaging and compressed sensing has grown, performing MRI reconstruction using model-based image reconstruction (MBIR)[25] has grown in popularity. MBIR has the advantage that it can incorporate additional operations into a model of the MRI system beyond standard Fourier encoding, and many groups have found that incorporating a fieldmap into their imaging model can greatly aid in the reduction of B_0 artifacts. MBIR can also serve as the foundation for hybrid physics + machine learning approaches that combine an imaging physics model with learned parameters, often referred to as "unrolled" algorithms.[99]

In MBIR, a so-called "forward model" is created that mathematically describes the transform from an image in vector form, denoted as $\mathbf{x}$, to acquired data, $\mathbf{y}$, using a matrix that here we will denote as $\mathbf{A}$. This can be thought of as a linear algebra representation of Equation (3) where data from all timepoints has been combined into a single vector $\mathbf{y}$, and can be written as

$$\mathbf{y} = \mathbf{A}\mathbf{x}. \tag{22}$$

Note that we have changed the letters representing the image and data from Equation (3) to align with common linear algebra nomenclature. In the simplest optimization approach, once we have a forward model, we can then optimize for the image using a linear least squares fit (since the dominant noise in MRI is Gaussian) as follows:

$$\hat{\mathbf{x}} = \arg\min_{\mathbf{x}} \frac{1}{2}\|\mathbf{A}\mathbf{x} - \mathbf{y}\|_2^2 + \lambda R(\mathbf{x}) \tag{23}$$

where $R(\mathbf{x})$ is a regularizer chosen by the user, and λ is a tuning parameter to balance between the data fit term and the regularization. A common choice of regularizer in MRI is a total variation (TV) term, but there are many different options for regularizers and alternative optimization algorithms to linear least squares, as discussed in a recent overview by Fessler.[25]

In MRI, the simplest possible forward model would be to have $\mathbf{A}$ equal to a discrete Fourier transform matrix. Additional common terms that are added include multicoil sensitivity maps and undersampling operators. The addition of an off-resonance field map is more complex, as the way the off-resonance affects the encoding forward model changes with time, as is shown in the first exponential term in Equation (5), and it requires approximating the full forward model and applying corresponding optimization algorithms to leverage the efficiencies of these models. Solving a minimization problem of the form shown in this section, as well as the direct methods discussed in Section 5.3.1, are often referred to as "inverse problems", and there are extensive prior work and tools available for these types of problem that can be applied to MRI.

5.4.1 | Efficient approximation of an expanded $\mathbf{B}_0$ forward model

To fully model the off-resonance exponential term in Equation (5) in matrix form would be computationally prohibitive, but lower-order approximations of the exponential can be made to efficiently model off-resonance.[26] As described in prior work[86,87] and Equation (18), the exponential can be modeled as a summation of basis functions. Using discretized versions of the L basis functions (b_{il} and c_{lj}), the matrix vector multiplication of $\mathbf{Ax}$ at row i (i.e., k-space data point i) now becomes

$$[\mathbf{A}(\boldsymbol{\omega})\mathbf{x}]_i \approx \sum_{l=1}^{L} b_{il} \left[\sum_{j=1}^{N} (x_j c_{lj}) e^{-i2\pi(\mathbf{k}_i \cdot \mathbf{r}_j)} \right] \tag{24}$$

where x_j is the magnetization (image value) at voxel index j, N is the number of voxels, $\mathbf{k}_i \cdot \mathbf{r}_j$ is the inner product of the ith k-space sampling location with the image space location of the jth voxel index, and $\mathbf{A}(\boldsymbol{\omega})$ denotes that $\mathbf{A}$ now contains the fieldmap. Here, $\mathbf{A}(\boldsymbol{\omega})$ is implemented efficiently with L NUFFTs. Additionally one can expand this to jointly optimize for the image and the fieldmap, assuming there is enough temporal variation in the k-space samples:

$$\hat{\mathbf{x}}, \hat{\boldsymbol{\omega}} = \arg\min_{\mathbf{x}, \boldsymbol{\omega}} \frac{1}{2} \|\mathbf{A}(\boldsymbol{\omega})\mathbf{x} - \mathbf{y}\|_2^2 + \lambda_1 R(\mathbf{x}) + \lambda_2 R(\boldsymbol{\omega}). \tag{25}$$

Sutton et al. performed this type of joint optimization using a spiral-in/spiral-out k-space trajectory[100] to calculate the fieldmap at every timepoint in an fMRI timeseries, allowing for dynamic B_0 correction of respiration-induced phase oscillations. Recent work has also incorporated multicoil information to aid in the joint reconstruction of the fieldmap and image using undersampled spiral-out and EPI trajectories.[101]

Other works have expanded the forward model $\mathbf{A}(\boldsymbol{\omega})$ to allow for a more accurate imaging model. Joint optimization of the fieldmap and R_2^* values has been performed to acquire quantitative BOLD information.[102] The imaging model can also be expanded to describe the differences in signal between water and fat, and to jointly optimize for water images, fat images, and the B_0 map.[103] More recently, a method to model through-voxel dephasing has been presented, which uses the gradient of the fieldmap within each voxel to estimate dephasing and recover lost signal.[104]

In addition to joint optimization, it is also possible to incorporate information from external sensors such as NMR probes to dynamically model the B_0 changes that occur during an MRI scan.[105] This dynamic B_0 tracking approach has recently allowed the acquisition of 0.8 mm × 0.8 mm resolution brain imaging with a 23 cm FOV at 7 T by using field probes during the 57 ms long single-shot spiral readouts,[106] which would produce severe artifacts without B_0 modeling.

Even with fast approximations, it should be noted that MBIR generally takes longer to run than direct approaches such as CP due to its iterative nature, and can also be more complex to implement. That said, the potential improvement can be substantial, and the utility of MBIR's improved accuracy will depend on the application and requirements of the imaging protocol (i.e., reconstruction time).

5.4.2 | Model-based reconstruction for low field

MBIRs have also proven valuable at low field, including recently published results showing improved *in vivo* human brain images from a portable low-field scanners using MBIR.[21,84] In the work of Koolstra et al., the forward model includes a B_0 fieldmap in a CP reconstruction as well as in an MB reconstruction (see Figure 9). Additionally, they model gradient nonlinearities. While not the focus of this paper, gradient nonlinearities can be important to incorporate at low field, and these are actually the terms that are modeled in the MBIR of the low-field work by Cooley et al,[21] not the B_0 field itself. Inclusion of gradient nonlinearities in the model will affect the k-space encoding term in equation 24, and shows the flexibility of the MBIR approach and the benefits of using it at low field.

5.5 | Dynamic correction and motion considerations

Dynamic off-resonance correction models the time-varying changes in the B_0 field during a scan, modeling the temporal updates using either a low-rank spatial representation of the field (i.e., spherical harmonics) or an entire fieldmap. Dynamic B_0 correction can be done either prospectively, where the B_0 field is updated during the scan (this is often referred to as dynamic shimming), or retrospectively, where different frames (e.g., individual frames in an fMRI timeseries or diffusion images at different b-values) are reconstructed assuming a different fieldmap.

For prospective correction, dynamic shimming can be done either in a volumetric approach, where the shim is updated during the scan to optimize homogeneity over the whole region of interest (this will require real time measurement of the B_0 field changes), or in a slice-by-slice

manner, where the optimal shims for each slice are determined, and then the shims are updated during the scan depending on which slice is being acquired (one can measure and dynamically update slice shims in real time, or optimal slice shims are determined prior to the experiment). Prospective correction without spatial information can also be useful to dynamically measure and update the center B_0 frequency in real time, for example in applications such as interventional MRI[107] and oscillating steady state imaging (OSSI) fMRI,[108] which has been shown to be very B_0 sensitive.[109]

In terms of hardware to update the shims, one option is to use built-in scanner shim coils (separate from the gradient coils), which generally shim up to first or second order but can go up to third order on some ultra-high-field systems. When using built-in shim coils, eddy currents should be taken into consideration as those can cause artifacts, and there are also potentially limits on the speed at which the shims can be updated using those coils. There are also more recent methods that dynamically shim using multicoil receive arrays that can also generate a DC current,[110,111] one of which by Stockmann et al. is aptly named an "AC/DC" coil. These methods take advantage of the higher-order shim fields generated from a multicoil array, due to it being located much closer to the object than scanner shim coils and having more elements to fine tune a desired field shape.

Retrospective approaches have also proven useful, and are helpful when dealing with motion during a scan. When a subject moves within the scanner, it will often result in a change of the B_0 fieldmap, requiring dynamic distortion correction. In diffusion MRI, techniques have been developed to correct for both motion changes and distortion changes during data acquisition.[112,113] Dynamic distortion correction is also important in fMRI experiments, and many groups have shown the benefits of estimating B_0 dynamically, using either raw k-space data[100] or phase measurements from the images themselves[114,115] or from multicoil FID measurements,[116] and then using the information in the reconstruction. Additionally, the potential clinical benefit of dynamic off-resonance correction has been shown in the application of presurgical fMRI at 7 T.[117]

Dynamic B_0 correction is also relevant in low-field imaging, especially in permanent magnet designs where there can be field drift during a scan.[19,22,28] In these approaches, a field probe or other methods are used to monitor drift during the acquisition, and then these measurements are used during the image reconstruction. At the other end of the field spectrum, dynamic B_0 correction has proven useful at ultra-high field, where there are large susceptibility artifacts.[35,118,119]

In MRS, which is very sensitive to off-resonance artifacts,[73] dynamic shimming is also very helpful. Spinal cord fMRI, including combined brain + spinal cord fMRI, can also benefit from dynamic shimming, because the effects of respiratory-induced magnetic susceptibility changes are much more severe when imaging closer to the lungs.[120,121] Finally, in applications such as speech MRI, where the data is inherently time varying, dynamic B_0 correction is important, since the B_0 field pattern will change as a subject speaks during the examination.[95,97,122]

5.6 | Correction for metal artifacts

As described above, the source of B_0 distortions around metal implants is largely the same as other sources of susceptibility-induced B_0 shifts, but larger in magnitude. Most imaging around implants uses spin echo (and variants) and traditional spin-warp-type acquisitions. This has the benefit of there being no geometric distortion in the PE direction, but still leaves artifacts in the readout and slice selection directions. The first step to minimize artifacts is to maximize the bandwidth per resolution element in each case, by increasing the receiver bandwidth for frequency encoding readouts and increasing the RF pulse bandwidth. While both have costs, these are useful strategies for reducing distortions. Similarly, one can use geometric distortion correction methods, such as fieldmap-based methods and others described above in Section 5.2.1, but these are ineffective for many of the larger distortions seen with metal implants.

5.6.1 | View angle tilting (VAT)

One clever approach for reducing in-plane distortions in the frequency direction is VAT.[123] Note that slices are shifted during the slice excitation, and shifted in the slice direction by an amount proportional to the B_0-induced frequency shift. Similarly, during frequency encoding the voxels are shifted in the readout direction proportional to this frequency shift. The VAT works by applying the slice select gradient again during frequency encoding. If the slice gradient is of the same amplitude as that used during excitation, then spins will be centered at the slice resonant frequency and not the original frequency shift. As a result, the frequency encoding sees the correct frequency associated with each spatial location along the read direction and distortions are removed. While effective, this approach is somewhat limited in that the frequency encoding should be about the same length as the RF pulse, which unfortunately makes the readouts very short at the expense of SNR. One could use a longer (narrow-bandwidth) RF pulse, but this leads to the slices being shifted by even larger amounts, so generally high-bandwidth RF pulses and frequency encoding are used. The main limitation of VAT is the residual and uncorrected distortion in the slice direction.

5.6.2 | Robust methods for distortion correction

The extreme challenge of large B_0 shifts around metal implants has led to several new methods for encoding images and the frequency offsets at the same time. One popular method is called multiacquisition variable-resonance image combination (MAVRIC),[124] in which slices are not excited at all, but rather narrow frequency bands are excited. Since there is no slice selection, 3D encoding is required to prevent aliasing in slice and PE directions. This is usually combined with fast spin echo/turbo spin echo methods to improve acquisition speed. Because a narrow band of frequency is excited, there is limited distortion of the images, governed by the readout bandwidth per pixel. To fill in the image holes, many (often overlapping) frequency bands must be excited and for each the exact shift correction for the frequency offset is applied. This creates many 3D volumes, which are then combined to create a volume that is undistorted in all three dimensions. The disadvantage of this approach is that it has poor SNR efficiency because shifted frequency bands do not improve the SNR of other frequency bands.

As mentioned above, the main issue with VAT is that the slice distortions are not corrected. Another comprehensive approach for distortion correction that addresses this issue is called slice encoding for metal artifact correction (SEMAC),[125] in which 2D slices are excited, but for each a 3D acquisitions is acquired so the distorted 3D profile of each excited slice can be visualized. VAT is used to correct for in-plane distortion and the 3D shifts are spliced together into a fully corrected 3D volume. As with MAVRIC, the SNR efficiency of this method is poor. Figure 10 demonstrates how regular spin echo images are badly distorted in both in-plane and slice directions, how VAT mostly corrects for the in-plane distortions but not the slice direction effects, and that SEMAC corrects for both in-plane and slice distortions. There are MAVRIC–SEMAC hybrid approaches[126] as well that can improve image quality and efficiency.
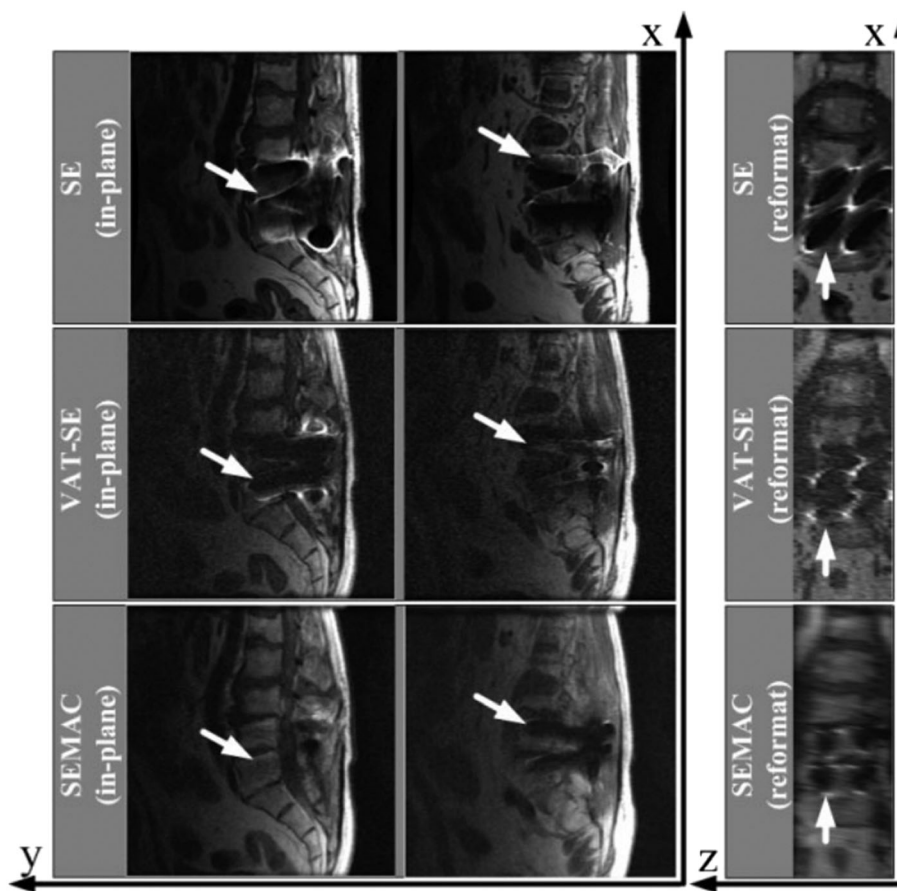
Lu, et al., Magnetic Resonance In Medicine, 2009

FIGURE 10   Comparison of standard spin echo imaging (top row), VAT (middle), and SEMAC (bottom row) methods for a patient with a spinal implant. The right-hand column is reformatted so that slice direction is along the horizontal axis. The spin echo image is badly distorted in both frequency and slice directions and the VAT images are partially corrected in the frequency direction with substantial slice distortion, while the SEMAC image is corrected in both directions. (Images reused from Reference [125] with permission.)

6 | CONCLUSIONS

Off-resonance artifacts are widespread in MRI, but fortunately there are many strategies to reduce and correct for them. Here we have described how off-resonance can originate from a variety of sources, such as inherent B_0 magnet inhomogeneity, magnetic susceptibility of tissue, chemical shift, and metallic implants. The effects of these inhomogeneities depend on the type of sequence used (spin echo versus gradient echo, Cartesian versus non-Cartesian) and therefore the correction strategies must be different as well. We have outlined the most common strategies for B_0 correction in Cartesian sequences (e.g., EPI), including fieldmap-based, TOPUP, and PSF approaches, as well as common strategies for non-Cartesian sequences (e.g., spiral), including direct (e.g., conjugate phase) and autofocusing methods. The effects and correction strategies for metallic implants also require a special approach, because of the very large magnetic susceptibility difference between metal and surrounding tissue. We have also discussed how model-based image reconstruction (MBIR) and dynamic correction can be used to correct for off-resonance in multiple types of sequence and application. Throughout, we have highlighted the ways in which low-field MRI can be easier to work with in terms of off-resonance effects (less magnetic susceptibility and chemical shift effects), how it can be more challenging (non-uniform B_0 field), and the substantial progress that has been made in correcting for B_0 effects at low field. Overall, the type of off-resonance artifact reduction and/or correction strategy will depend on the application, and future developments in the field of off-resonance correction will continue to enable new applications and use cases for MRI.

COMPETING INTEREST

Melissa W. Haskell is employed by Hyperfine, Inc.

ORCID

Melissa W. Haskell https://orcid.org/0000-0002-7237-6731

REFERENCES

1. Lüdeke KM, Röschmann P, Tischler R. Susceptibility artefacts in NMR imaging. *Magn Reson Imaging*. 1985;3(4):329-343.
2. O'Donnell M, Edelstein WA. NMR imaging in the presence of magnetic field inhomogeneities and gradient field nonlinearities. *Med Phys*. 1985;12(1):20-26.
3. Czervionke LF, Daniels DL, Wehrli FW, et al. Magnetic susceptibility artifacts in gradient-recalled echo MR imaging. *Am J Neuroradiol*. 1988;9(6):1149-1155.
4. Michiels J, Bosmans H, Pelgrims P, et al. On the problem of geometric distortion in magnetic resonance images for stereotactic neurosurgery. *Magn Reson Imaging*. 1994;12(5):749-765.
5. Ladd ME, Erhart P, Debatin JF, Romanowski BJ, Boesiger P, McKinnon GC. Biopsy needle susceptibility artifacts. *Magn Reson Med*. 1996;36(4):646-651.
6. Walker A, Liney G, Metcalfe P, Holloway L. MRI distortion: considerations for MRI based radiotherapy treatment planning. *Australas Phys Eng Sci Med*. 2014;37(1):103-113.
7. Weygand J, Fuller CD, Ibbott GS, et al. Spatial precision in magnetic resonance imaging-guided radiation therapy: the role of geometric distortion. *Int J Radiat Oncol Biol Phys*. 2016;95(4):1304-1316.
8. Hargreaves BA, Worters PW, Pauly KB, Pauly JM, Koch KM, Gold GE. Metal-induced artifacts in MRI. *Am J Roentgenol*. 2011;197(3):547-555.
9. Jezzard P, Stuart C. Sources of distortion in functional MRI data. *Hum Brain Mapp*. 1999;8(2/3):80-85.
10. Jezzard P. Correction of geometric distortion in fMRI data. *NeuroImage*. 2012;62(2):648-651.
11. Hahn EL. Spin echoes. *Phys Rev*. 1950;80(4):580-594.
12. Hennig J, Nauerth A, Friedburg H. RARE imaging: a fast imaging method for clinical MR. *Magn Reson Med*. 1986;3(6):823-833.
13. Larkman DJ, Atkinson D, Hajnal JV. Artifact reduction using parallel imaging methods. *Top Magn Reson Imaging*. 2004;15(4):267-275.
14. Feinberg DA, Setsompop K. Ultra-fast MRI of the human brain with simultaneous multi-slice imaging. *J Magn Reson*. 2013;229:90-100.
15. Stehling MK, Turner R, Mansfield P, Stehling MK. Echo-Planar Imaging: Magnetic Resonance Imaging in a Fraction of a Second. *Technical report*; 1991.
16. Kwong KK, Belliveau JW, Chesler DA, et al. Dynamic magnetic resonance imaging of human brain activity during primary sensory stimulation. *Proc Natl Acad Sci USA*. 1992;89(12):5675-5679.

17. Liu C, Li W, Tong KA, Yeom KW, Kuzminski S. Susceptibility-weighted imaging and quantitative susceptibility mapping in the brain. *J Magn Reson Imaging*. 2015;42(1):23-41.

18. Duyn JH, Schenck J. Contributions to magnetic susceptibility of brain tissue. *NMR Biomed*. 2017;30(4):e3546.

19. Nakagomi M, Kajiwara M, Matsuzaki J, et al. Development of a small car-mounted magnetic resonance imaging system for human elbows using a 0.2 T permanent magnet. *J Magn Reson*. 2019;304:7.

20. Liu Y, Leong AT, Zhao Y, et al. A low-cost and shielding-free ultra-low-field brain MRI scanner. *Nat Commun*. 2021;12(1):1-14.

21. Cooley CZ, McDaniel PC, Stockmann JP, et al. A portable scanner for magnetic resonance imaging of the brain. *Nat Biomed Eng*. 2021;5(3):229-239.

22. O'Reilly T, Teeuwisse WM, de Gans D, Koolstra K, Webb AG. In vivo 3D brain and extremity MRI at 50 mT using a permanent magnet Halbach array. *Magn Reson Med*. 2021;85(1):495-505.

23. Sheth KN, Mazurek MH, Yuen MM, et al. Assessment of brain injury using portable, low-field magnetic resonance imaging at the bedside of critically ill patients. *JAMA Neurol*. 2021;78(1):41-47.

24. Geethanath S, Vaughan JT Jr. Accessible magnetic resonance imaging: a review. *J Magn Reson Imaging*. 2019;49(7):e65-e77.

25. Fessler JA. Optimization methods for magnetic resonance image reconstruction: key models and optimization algorithms. *IEEE Signal Process Mag*. 2020;37(1):33-40.

26. Sutton BP, Noll DC, Fessler JA. Fast, iterative image reconstruction for MRI in the presence of field inhomogeneities. *IEEE Trans Med Imaging*. 2003; 22(2):178-188.

27. Fessler JA. Michigan Image Reconstruction Toolbox. 2022. https://web.eecs.umich.edu/~fessler/code

28. Cooley CZ, Stockmann JP, Armstrong BD, et al. Two-dimensional imaging in a lightweight portable MRI scanner without gradient coils. *Magn Reson Med*. 2014;883:872-883.

29. Cooley CZ, Haskell MW, Cauley SF, et al. Design of sparse Halbach magnet arrays for portable MRI using a genetic algorithm. *IEEE Trans Magn*. 2018;54(1):1-12.

30. O'Reilly T, Teeuwisse WM, Webb AG. Three-dimensional MRI in a homogenous 27 cm diameter bore Halbach array magnet. *J Magn Reson*. 2019; 307:106578.

31. McDaniel PC, Cooley CZ, Stockmann JP, Lawrence LW. The MR cap: a single-sided MRI system designed for potential point-of-care limited field-of-view brain imaging. *Magn Reson Med*. 2019;82(5):1946-1960.

32. Obungoloch J, Harper JR, Consevage S, et al. Design of a sustainable prepolarizing magnetic resonance imaging system for infant hydrocephalus. *Magn Reson Mater Phys Biol Med*. 2018;31(5):665-676.

33. Schenck JF. The role of magnetic susceptibility in magnetic resonance imaging: MRI magnetic compatibility of the first and second kinds. *Med Phys*. 1996;23(6):815-850.

34. Farahani K, Sinha U, Sinha S, Chiu LCL, Lufkin RB. Effect of field strength on susceptibility artifacts in magnetic resonance imaging. *Comput Med Imaging Graph*. 1990;14(6):409-413.

35. Stockmann JP, Wald LL. In vivo B_0 field shimming methods for MRI at 7 T. *NeuroImage*. 2018;168:71-87.

36. Elster AD. 2022. https://mriquestions.com/what-is-susceptibility.html

37. Hood MN, Ho VB, Smirniotopoulos JG, Jerzy S. Chemical shift: the artifact and clinical tool revisited. *RadioGraphics*. 1999;19(2):357-371.

38. Babcock EE, Brateman L, Weinreb JC, Horner SD, Ray LN. Edge artifacts in MR images: chemical shift effect. *J Comput Assist Tomogr*. 1985;9(2): 252-257.

39. Dwyer AJ, Knop RH, Hoult DI. Frequency shift artifacts in MR imaging. *J Comput Assist Tomogr*. 1985;1(1):16-18.

40. Smith RC, Lange RC, McCarthy SM. Chemical shift artifact: dependence on shape and orientation of the lipid-water interface. *Radiology*. 1991;10(1): 225-229.

41. ASTM. ATSM F2503-13: Standard practice for marking medical devices and other items for safety in the magnetic resonance environment. *Technical report*, West Conshohocken, PA, USA, American Society for Testing and Materials International; 2013.

42. IEC. IEC 62570:2014: Standard practice for marking medical devices and other items for safety in the magnetic resonance environment. *Technical report*, Geneva, Switzerland, International Electrotechnical Commission; 2014.

43. Jungmann PM, Agten CA, Pfirrmann CW, Reto S. Advances in MRI around metal. *J Magn Reson Imaging*. 2017;46(4):972-991.

44. Van Speybroeck CDE, O'Reilly T, Teeuwisse W, Arnold PM, Webb AG. Characterization of displacement forces and image artifacts in the presence of passive medical implants in low-field (¡100 mT) permanent magnet-based MRI systems, and comparisons with clinical MRI systems. *Phys Med*. 2021;84(February):116-124.

45. Wang D, David D. Geometric distortion in structural magnetic resonance imaging. *Curr Med Imaging Rev*. 2005;1(1):49-60.

46. Macovski A. Noise in MRI. *Magn Reson Med*. 1996;36(3):494-497.

47. Porter D, Mueller E. Multi-shot diffusion-weighted EPI with readout mosaic segmentation and 2D navigator correction. In: Proceedings of the 12th Annual Meeting of ISMRM; 2004; Kyoto:442.

48. Holdsworth SJ, Skare S, Newbould RD, Guzmann R, Blevins NH, Bammer R. Readout-segmented EPI for rapid high resolution diffusion imaging at 3 T. *Eur J Radiol*. 2008;65(1):36-46.

49. Butts K, Crespigny A, Pauly JM, Michael M. Diffusion-weighted interleaved echo-planar imaging with a pair of orthogonal navigator echoes. *Magn Reson Med*. 1996;35(5):763-770.

50. Noll DC. Multishot rosette trajectories for spectrally selective MR imaging. *IEEE Trans Med Imaging*. 1997;16(4):372-377.

51. Weiger M, Brunner DO, Dietrich BE, Müller CF, Pruessmann KP. ZTE imaging in humans. *Magn Reson Med*. 2013;70(2):328-332.

52. Gatehouse PD, Bydder GM. Magnetic resonance imaging of short T_2 components in tissue. *Clin Radiol*. 2003;58(1):1-19.

53. Jiang D, Carroll TJ, Brodsky E, et al. Contrast-enhanced peripheral magnetic resonance angiography using time-resolved vastly undersampled isotropic projection reconstruction. *J Magn Reson Imaging*. 2004;20(5):894-900.

54. Li F, Grimm R, Block KT, et al. Golden-angle radial sparse parallel MRI: combination of compressed sensing, parallel imaging, and golden-angle radial sampling for fast and flexible dynamic volumetric MRI. *Magn Reson Med*. 2014;72(3):707-717.

55. Noll DC, Cohen JD, Meyer CH, Schneider W. Spiral *k*-space MR imaging of cortical activation. *J Magn Reson Imaging*. 1995;5(1):49-56.

56. Nayak KS, Hargreaves BA, Bob S, Nishimura DG, Pauly JM, Meyer CH. Spiral balanced steady-state free precession cardiac imaging. *Magn Reson Med*. 2005;53(6):1468-1473.

57. Li Z, Pipe JG, Ooi MB, Kuwabara M, Karis JP. Improving the image quality of 3D FLAIR with a spiral MRI technique. *Magn Reson Med*. 2020;83(1): 170-177.

58. Irarrazabal P, Nishimura DG. Fast three dimensional magnetic resonance imaging. *Magn Reson Med*. 1995;33(5):656-662.

59. Hutton C, Bork A, Josephs O, Deichmann R, Ashburner J, Robert T. Image distortion correction in fMRI: a quantitative evaluation. *NeuroImage*. 2002; 16(1):217-240.

60. Reber PJ, Wong EC, Buxton RB, Frank LR. Correction of off resonance-related distortion in echo-planar imaging using EPI-based field maps. *Magn Reson Med*. 1998;39(2):328-330.

61. Jenkinson M, Beckmann CF, Behrens TE, Woolrich MW, Smith SM. FSL. *NeuroImage*. 2012;62(2):782-790.

62. Jenkinson M. Fast, automated, *N*-dimensional phase-unwrapping algorithm. *Magn Reson Med*. 2003;49(1):193-197.

63. Iyer SS, Liao C, Li Q, et al. PhysiCal: A rapid calibration scan for B_0, B_1^+, coil sensitivity and eddy current mapping. In: Proceedings of the 28th Annual Meeting of ISMRM Sydney/Virtual; 2020:661.

64. Barmet C, Zanche ND, Pruessmann KP. Spatiotemporal magnetic field monitoring for MR. *Magn Reson Med*. 2008;60(1):187-197.

65. Dietrich BE, Brunner DO, Wilm BJ, et al. A field camera for MR sequence monitoring and system analysis. *Magn Reson Med*. 2016;75(4):1831-1840.

66. Gross S, Barmet C, Dietrich BE, Brunner DO, Schmid T, Pruessmann KP. Dynamic nuclear magnetic resonance field sensing with part-per-trillion resolution. *Nat Commun*. 2016;7:1-6.

67. Wallace TE, Afacan O, Kober T, Warfield SK. Rapid measurement and correction of spatiotemporal B_0 field changes using FID navigators and a multi-channel reference image. *Magn Reson Med*. 2020;83(2):575-589.

68. Jezzard P, Balaban RS. Correction for geometric distortion in echo planar images from B_0 field variations. *Magn Reson Med*. 1995;34(1):65-73.

69. Funai AK, Fessler JA, Yeo DTB, Noll DC, Olafsson VT. Regularized field map estimation in MRI. *IEEE Trans Med Imaging*. 2008;27(10):1484-1494.

70. Lin CY, Fessler JA. Efficient regularized field map estimation in 3D MRI. *IEEE Trans Comput Imaging*. 2020;6(1):1451-1458.

71. Andersson JLR, Skare S, John A. How to correct susceptibility distortions in spin-echo echo-planar images: application to diffusion tensor imaging. *NeuroImage*. 2003;20(2):870-888.

72. Schneider E, Gary G. Rapid in vivo proton shimming. *Magn Reson Med*. 1991;18(2):335-347.

73. Juchem C, Cudalbu C, Graaf RA, et al. B_0 shimming for in vivo magnetic resonance spectroscopy: experts' consensus recommendations. *NMR Biomed*. 2021;34(5):1-20.

74. Larkman DJ, Nunes RG. Parallel magnetic resonance imaging. *Phys Med Biology*. 2007;52(7):15-55.

75. Bley TA, Wieben O, François CJ, Brittain JH, Reeder SB. Fat and water magnetic resonance imaging. *J Magn Reson Imaging*. 2010;31(1):4-18.

76. Schallmo MP, Weldon KB, Burton PC, Sponheim SR, Olman CA. Assessing methods for geometric distortion compensation in 7 T gradient echo functional MRI data. *Hum Brain Mapp*. 2021;42(13):4205-4223.

77. Abreu R, Duarte JV. Quantitative assessment of the impact of geometric distortions and their correction on fMRI data analyses. *Front Neurosci*. 2021;15:1-17.

78. Robson MD, Gore JC, Constable RT. Measurement of the point spread function in MRI using constant time imaging. *Magn Reson Med*. 1997;38(5): 733-740.

79. Zeng H, Constable RT. Image distortion correction in EPI: comparison of field mapping with point spread function mapping. *Magn Reson Med*. 2002; 48(1):137-146.

80. Zaitsev M, Hennig J, Speck O. Point spread function mapping with parallel imaging techniques and high acceleration factors: fast, robust, and flexible method for echo-planar imaging distortion correction. *Magn Reson Med*. 2004;52(5):1156-1166.

81. Fessler JA. On NUFFT-based gridding for non-Cartesian MRI. *J Magn Reson*. 2007;188(2):191-195.

82. Macovski A. Volumetric NMR imaging with time-varying gradients. *Magn Reson Med*. 1985;2(1):29-40.

83. Maeda A, Sano K, Yokoyama T. Reconstruction by weighted correlation for MRI with time-varying gradients. *IEEE Trans Med Imaging*. 1988;7(1): 26-31.

84. Koolstra K, O'Reilly T, Börnert P, Webb A. Image distortion correction for MRI in low field permanent magnet systems with strong B_0 inhomogeneity and gradient field nonlinearities. *Magn Reson Mater Phys Biol Med*. 2021;34(4):631-642.

85. Noll DC, Fessler JA, Sutton BP. Conjugate phase MRI reconstruction with spatially variant sample density correction. *IEEE Trans Med Imaging*. 2005; 24(3):325-336.

86. Fessler JA, Lee S, Olafsson VT, Shi HR, Noll DC. Toeplitz-based iterative image reconstruction for MRI with correction for magnetic field inhomogeneity. *IEEE Trans Signal Process*. 2005;53(9):3393-3402.

87. Fessler J. Model-based image reconstruction for MRI. *IEEE Signal Process Mag*. 2010;27(4):81-89.

88. Noll DC, Meyer CH, Pauly JM, Nishimura DG, Albert M. A homogeneity correction method for magnetic resonance imaging with time-varying gradients. *IEEE Trans Med Imaging*. 1991;10(4):629-637.

89. Noll DC. Reconstruction techniques for magnetic resonance imaging. *PhD thesis*: Stanford University; 1991.

90. Man LC, Pauly JM, Macovski A. Multifrequency interpolation for fast off-resonance correction. *Magn Reson Med*. 1997;37(5):785-792.

91. Ahunbay E, Pipe JG. Rapid method for deblurring spiral MR images. *Magn Reson Med*. 2000;44(3):491-494.

92. Kadah YM, Xiaoping H. Simulated phase evolution rewinding (SPHERE): a technique for reducing B_0 inhomogeneity effects in MR images. *Magn Reson Med*. 1997;38(4):615-627.

93. Schomberg H. Off-resonance correction of MR images. *IEEE Trans Med Imaging*. 1999;18(6):481-495.

94. Noll DC, Pauly JM, Meyer CH, Nishimura DG, Albert M. Deblurring for non-2D Fourier transform magnetic resonance imaging. *Magn Reson Med*. 1992;25(2):319-333.

95. Lim Y, Lingala SG, Narayanan SS, Nayak KS. Dynamic off-resonance correction for spiral real-time MRI of speech. *Magn Reson Med*. 2019;81(1): 234-246.

96. Zeng DY, Shaikh J, Holmes S, et al. Deep residual network for off-resonance artifact correction with application to pediatric body MRA with 3D cones. *Magn Reson Med*. 2019;82(4):1398-1411.

97. Lim Y, Bliesener Y, Narayanan S, Nayak KS. Deblurring for spiral real-time MRI using convolutional neural networks. *Magn Reson Med*. 2020;84(6): 3438-3452.

98. Haskell MW, Lahiri A, Nielsen J-F, Fessler JA, Douglas CN. FieldMapNet MRI: learning-based mapping from single echo time BOLD fMRI data to fieldmaps with model-based reconstruction. In: Proceedings of the 30th Annual Meeting of ISMRM; 2022; London:235.

99. Liang D, Cheng J, Ke Z, Leslie Y. Deep magnetic resonance image reconstruction: inverse problems meet neural networks. *IEEE Signal Process Mag*. 2020;37(1):141-151.

100. Sutton BP, Noll DC, Fessler JA. Dynamic field map estimation using a spiral-in/spiral-out acquisition. *Magn Reson Med*. 2004;51(6):1194-1204.

101. Patzig F, Wilm B, Pruessmann KP. Off-resonance self-correction by implicit B_0-encoding. In: Proceedings of the 29th Annual Meeting of ISMRM Virtual; 2021:666.

102. Olafsson VT, Noll DC, Fessler JA. Fast joint reconstruction of dynamic R_2^* and field maps in functional MRI. *IEEE Trans Med Imaging*. 2008;27(9):1177-1188.

103. Hernando D, Haldar JP, Sutton BP, Ma J, Kellman P, Liang Z.-P. Joint estimation of water/fat images and field inhomogeneity map. *Magn Reson Med*. 2008;59(3):571-580.

104. Lam F, Sutton BP, Intravoxel B_0 inhomogeneity corrected reconstruction using a low-rank encoding operator. *Magn Reson Med*. 2020;84(2):885-894.

105. Wilm BJ, Barmet C, Pavan M, Pruessmann KP, Higher order reconstruction for MRI in the presence of spatiotemporal field perturbations. *Magn Reson Med*. 2011;65(6):1690-1701.

106. Kasper L, Engel M, Heinzle J, et al. Advances in spiral fMRI: a high-resolution study with single-shot acquisition. *NeuroImage*. 2022;246:118738.

107. Campbell-Washburn AE, Xue H, Lederman RJ, Faranesh AZ, Hansen MS. Real-time distortion correction of spiral and echo planar images using the gradient system impulse response function. *Magn Reson Med*. 2016;75(6):2278-2285.

108. Cao AA, Douglas N. Real-time respiration compensation in oscillating steady state fMRI. In: Proceedings of the 28th Annual Meeting of ISMRM, Sydney/Virtual; 2020:1223.

109. Guo S, Douglas CN. Oscillating steady-state imaging (OSSI): a novel method for functional MRI. *Magn Reson Med*. 2020;84(2):698-712.

110. Stockmann JP, Witzel T, Keil B, et al. A 32-channel combined RF and B_0 shim array for 3 T brain imaging. *Magn Reson Med*. 2016;75(1):441-451.

111. Darnell D, Truong TK, Song AW. Integrated parallel reception, excitation, and shimming (iPRES) with multiple shim loops per radio-frequency coil element for improved B_0 shimming. *Magn Reson Med*. 2017;77(5):2077-2086.

112. Andersson JLR, Graham MS, Drobnjak I, Zhang H, Jon C. Susceptibility-induced distortion that varies due to motion: correction in diffusion MR without acquiring additional data. *NeuroImage*. 2018;171:277-295.

113. Hutter J, Christiaens DJ, Schneider T, et al. Slice-level diffusion encoding for motion and distortion correction. *Med Image Anal*. 2018;48:214-229.

114. Hahn AD, Nencka AS, Rowe DB. Improving robustness and reliability of phase-sensitive fMRI analysis using temporal off-resonance alignment of single-echo timeseries (TOAST). *NeuroImage*. 2009;44(3):742-752.

115. Dymerska B, Poser BA, Barth M, Trattnig S, Robinson SD. A method for the dynamic correction of B_0-related distortions in single-echo EPI at 7 T. *NeuroImage*. 2018;168:321-331.

116. Wallace TE, Polimeni JR, Stockmann JP, et al. Dynamic distortion correction for functional MRI using FID navigators. *Magn Reson Med*. 2021;85(3):1294-1307.

117. Cardoso PL, Dymerska B, Bachratá B, et al. The clinical relevance of distortion correction in presurgical fMRI at 7 T. *NeuroImage*. 2018;168(December 2016):490-498.

118. Juchem C, Nixon TW, Diduch P, Rothman DL, Starewicz P, De Graaf RA. Dynamic shimming of the human brain at 7 T. *Concepts Magn Reson B*. 2010;37(3):116-128.

119. Sengupta S, Brian Welch E, Zhao Y, et al. Dynamic B_0 shimming at 7 T. *Magn Reson Imaging*. 2011;29(4):483-496.

120. Finsterbusch J, Sprenger C, Büchel C. Combined T_2^*-weighted measurements of the human brain and cervical spinal cord with a dynamic shim update. *NeuroImage*. 2013;79:153-161.

121. Islam H, Law CSW, Weber KA, Mackey SC, Glover GH. Dynamic per slice shimming for simultaneous brain and spinal cord fMRI. *Magn Reson Med*. 2019;81(2):825-838.

122. Lingala SG, Sutton BP, Miquel ME, Nayak KS. Recommendations for real-time speech MRI. *J Magn Reson Imaging*. 2016;43(1):28-44.

123. Kolind SH, MacKay AL, Munk PL, Xiang QS. Quantitative evaluation of metal artifact reduction techniques. *J Magn Reson Imaging*. 2004;20(3):487-495.

124. Koch KM, Lorbiecki JE, Scott Hinks R, King KF. A multispectral three-dimensional acquisition technique for imaging near metal implants. *Magn Reson Med*. 2009;61(2):381-390.

125. Wenmiao L, Pauly KB, Gold GE, Pauly JM, Brian AH. SEMAC: slice encoding for metal artifact correction in MRI. *Magn Reson Med*. 2009;62(1):66-76.

126. Koch KM, Brau AC, Chen W, et al. Imaging near metal with a MAVRIC–SEMAC hybrid. *Magn Reson Med*. 2011;65(1):71-82.